Chemical Science

ROYAL SOCIETY OF CHEMISTRY

EDGE ARTICLE

View Article Online
View Journal | View Issue

Cite this: *Chem. Sci.*, 2024, **15**, 7982

All publication charges for this article have been paid for by the Royal Society of Chemistry

Received 15th March 2024
Accepted 23rd April 2024

DOI: 10.1039/d4sc01755b

rsc.li/chemical-science

Structural elucidation of HIV-1 G-quadruplexes in a cellular environment and their ligand binding using responsive ^{19}F-labeled nucleoside probes†

Sarupa Roy,[a] Priyasha Majee,[b] Sruthi Sudhakar,[b] Satyajit Mishra,[c] Jeet Kalia,[cd] P. I. Pradeepkumar *[b] and Seergazhi G. Srivatsan *[a]

Understanding the structure and recognition of highly conserved regulatory segments of the integrated viral DNA genome that forms unique topologies can greatly aid in devising novel therapeutic strategies to counter chronic infections. In this study, we configured a probe system using highly environment-sensitive nucleoside analogs, 5-fluoro-2′-deoxyuridine (FdU) and 5-fluorobenzofuran-2′-deoxyuridine (FBFdU), to investigate the structural polymorphism of HIV-1 long terminal repeat (LTR) G-quadruplexes (GQs) by fluorescence and ^{19}F NMR. FdU and FBFdU, serving as hairpin and GQ sensors, produced distinct spectral signatures for different GQ topologies adopted by LTR G-rich oligonucleotides. Importantly, systematic ^{19}F NMR analysis in *Xenopus laevis* oocytes gave unprecedented information on the structure adopted by the LTR G-rich region in the cellular environment. The results indicate that it forms a unique GQ-hairpin hybrid architecture, a potent hotspot for selective targeting. Furthermore, structural models generated using MD simulations provided insights on how the probe system senses different GQs. Using the responsiveness of the probes and *Taq* DNA polymerase stop assay, we monitored GQ- and hairpin-specific ligand interactions and their synergistic inhibitory effect on the replication process. Our findings suggest that targeting GQ and hairpin motifs simultaneously using bimodal ligands could be a new strategy to selectively block the viral replication.

Introduction

HIV-1 is one of the most lethal retroviruses, which induces a chronic infection by etching the host cell genome with a proviral DNA that is reverse transcribed from its RNA genome. Established treatments use a cocktail of drugs having different modes of action to control the disease progression.[1] However, due to persistence of latent reservoirs, drug-resistance and promiscuity of the viral polymerase, it is very hard to eradicate the virus completely from the host system.[2,3] One of the current ways to counter latency involves awakening dormant viruses and simultaneously inhibiting viral replication with antiviral agents.[4,5] It is also hypothesized that targeting certain structural and functional segments of the integrated viral DNA genome could complement the above strategy and help in curing the disease.[6] An important and a highly conserved gene segment that could be suitable for this purpose is the long terminal repeat (LTR) of the HIV-1 promoter region.[7,8]

The initiation of HIV-1 transcription is navigated by the promoter region 5′-LTR, which is composed of U3, R and U5 regions.[9] The U3 region consists of three functional segments including the highly conserved core-binding site of NF-κB and Sp1 transcription factors,[10] which harbors contiguous G-rich tracts capable of forming G-quadruplex (GQ) structures namely LTR-II, LTR-III and LTR-IV, and HIVpro1 and HIVpro2 (Fig. 1A).[11–13] Notably, LTR-III and LTR-IV form GQs *in vitro* in a mutually exclusive manner. While LTR-III adopts a unique architecture made of a hybrid-type GQ juxtaposed with a three G-C paired hairpin motif, LTR-IV attains a parallel GQ topology with a T-bulge (Fig. 1B).[14,15] However, the entire G-rich region majorly forms the GQ-hairpin form like the LTR-III motif, and the parallel form of LTR-IV is induced when it binds to ligands or protein factors.[14–16] Importantly, the LTR GQ region represents an evolutionary conserved element across all primate lentiviruses, and the balance between different GQ structures is implicated in the propagation and latency of the virus.[17,18]

[a]*Department of Chemistry, Indian Institute of Science Education and Research (IISER), Pune, Dr Homi Bhabha Road, Pune 411008, India. E-mail: srivatsan@iiserpune.ac.in*

[b]*Department of Chemistry, Indian Institute of Technology Bombay, Mumbai 400076, India. E-mail: pradeep@chem.iitb.ac.in*

[c]*Department of Biological Sciences, Indian Institute of Science Education and Research (IISER) Bhopal, Bhopal Bypass Road, Bhauri, Bhopal 462066, India*

[d]*Department of Chemistry, Indian Institute of Science Education and Research (IISER) Bhopal, Bhopal Bypass Road, Bhauri, Bhopal 462066, India*

† Electronic supplementary information (ESI) available: Experimental details, CD, T_m, fluorescence, MD simulation, mass, NMR spectra and gel images. Experimental procedure for NMR measurements of ONs in a cellular environment, and ligand interaction with LTR GQs and their effects on the *Taq* DNA polymerase activity are described. See DOI: https://doi.org/10.1039/d4sc01755b

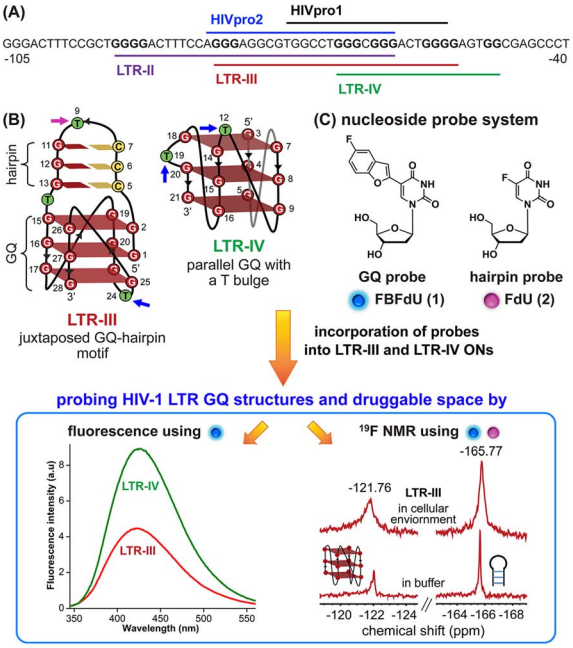

Fig. 1 (A) Schematic representation of the HIV-1 LTR G-rich region. (B) Secondary structures of LTR-III and LTR-IV GQs are depicted using the respective NMR structures (PDB: 6H1K and 2N4Y). (C) Environment-sensitive nucleoside system designed to probe the structural polymorphism and druggable space of LTR GQs by fluorescence and ^{19}F NMR techniques in cell-free and cellular environments. Potential sites for incorporation of the GQ probe (FBFdU **1**) and hairpin probe (FdU **2**) into the loop region of LTR-III and LTR-IV G-rich sequences are shown with blue and magenta arrows, respectively.

Therefore, we envision that the virus status can be selectively controlled in the host cell by using structure-specific binders. In this direction, it is important to gain a comprehensive understanding of the structural polymorphism, dynamics and druggable space of LTR GQs in a cellular environment to advocate a viable therapeutic strategy.

A multitude of biophysical and biochemical techniques including CD, UV thermal melting, fluorescence, NMR and X-ray crystallography add pieces of valuable information to characterize GQs *in vitro*.[19–25] Recently, antibodies and chemical probes have been developed to detect ensembles of DNA GQs in cells.[26–30] However, the majority of tools fall short when evaluating co-existing structures, as the challenges are twofold: (i) inability to differentiate different GQ topologies (exceptions are few)[31–34] and (ii) limited capability to assess structures in a cellular environment. Also, sequences with multiple G tracts exhibit high structural polymorphism and dynamics, which can vary between cell-free and cellular environments.[35,36] Therefore, we sought to devise a probe platform that would (i) provide spectral signatures for different GQs formed by the LTR G-rich region, which could help identify the preferred GQ in cells and (ii) allow us to survey the chemical space of LTR GQs to design structure-specific binders.

In this context, we developed microenvironment-sensitive dual-functional nucleoside probes that immensely aid in studying nucleic acid conformations and topology-specific ligand/drug interaction.[37,38] In particular, 5-fluorobenzofuran-modified 2′-deoxyuridine (FBFdU) serves as an excellent two-channel readout system to detect different GQ conformations of the human telomeric repeat *in vitro* and in cellular milieu by using fluorescence and ^{19}F NMR techniques.[37] However, LTR-III forms a juxtaposed GQ-hairpin motif that is unique for the HIV-1 virus. Hence, we realized that by using only a GQ sensing probe (FBFdU) it would not be possible to survey the landscape of the LTR. In this regard, here we report the development of a probe system that uses FBFdU as a GQ sensor and 5-fluoro-2′-deoxyuridine (FdU) as a hairpin sensor (Fig. 1C). The probes judiciously placed in loop positions of the LTR G-rich region are minimally perturbing, and importantly, produce distinct and resolved spectral signatures for LTR-III and LTR-IV GQs. Rewardingly, we deduced the GQ structure adopted by the LTR promoter region in an *ex vivo* model (*Xenopus laevis* oocyte extract) by using ^{19}F NMR signatures obtained *in vitro*. Furthermore, the probe platform and *Taq* DNA polymerase assay helped in mapping ligand interactions and their influence on the LTR replication process.

Results and discussion

Structural investigation of the modified HIV-1 LTR by fluorescence and ^{19}F NMR *in vitro*

Design of the nucleoside probe platform. The loop orientation, composition and loop residue interaction with neighboring bases are very different amongst the GQs.[39,40] Environment-sensitive nucleoside analogs capable of sensing these differences act as good GQ probes.[41,42] Therefore, to configure a probe system, we decided to exploit the differences in the structural features of LTR GQs, particularly at the loop nucleoside level. A 28-mer ON **3** representing the LTR-III region adopts a parallel-antiparallel hybrid-type GQ structure comprising three stacked tetrads connected by four loops (Fig. 1B and Table 1).[14] The 12-nucleotide diagonal loop (3–14 residues) forms a juxtaposed hairpin motif wherein three G–C base pairs are capped by a loop formed by G_8–T_9–G_{10} residues. We envisioned that T_9, part of the hairpin loop and T_{24}, part of a 3-nt lateral loop (A_{22}–C_{23}–T_{24}) connecting the G-tetrads would be potential sites for placing nucleoside probes to distinguish hairpin and GQ motifs. On the other hand, LTR-IV ON **8** adopts an all-parallel stranded GQ with a T_{19} bulge that stacks with A_{17} of the propeller loop (Fig. 1B and Table 1). It is shown that T_{19} is not mandatory for GQ formation, and hence, placing a GQ sensor at this position should not affect the native GQ structure. Furthermore, a 4-nt propeller loop formed by A_{10}–C_{11}–T_{12}–G_{13} bases is also envisioned as a good location to place the probe.[15] Based on this key information, we used a combination of two highly conformation-sensitive nucleoside probes, FBFdU (GQ sensor)[37] and FdU (hairpin/duplex sensor),[43,44] to distinguish different structures adopted by the LTR G-rich region (Fig. 1B and C). A foreseeable advantage of this probe combination is that the chemical shift region of FBFdU (around −122 ppm) and FdU (around −165 ppm) is significantly different so that the individual domains can be unequivocally distinguished, which otherwise is difficult by other currently available tools (*vide infra*).

Table 1 Sequence of native and modified LTR ONs

G-rich domain	ON[a]	5′—3’
LTR-III	**3**	GGGAGGCGTGGCCTGGGCGGGACTGGGG
	4	GGGAGGCG**2**GGCCTGGGCGGGAC**1**GGGG
	5	GGGAGGCGTGGCCTGGGCGGGAC**1**GGGG
	6	GGGAGGCG**2**GGCCTGGGCGGGACTGGGG
	7	CCCCAGTCCCGCCCAGGCCACGCCTCCC
LTR-IV	**8**	CTGGGCGGGACTGGGGAGTGGT
	9	CTGGGCGGGAC**1**GGGGAGTGGT
	10	CTGGGCGGGACTGGGGAG**1**GGT
	11	ACCACTCCCCAGTCCCGCCCAG
LTR-III + IV	**12**	AGGGAGGCGTGGCCTGGGCGGGACTGGGGAGTGGT
	13	AGGGAGGCGTGGCCTGGGCGGGAC**1**GGGGAGTGGT
	14	AGGGAGGCGTGGCCTGGGCGGGACTGGGGAG**1**GGT
	15	AGGGAGGCG**2**GGCCTGGGCGGGACTGGGGAGTGGT
	16	AGGGAGGCG**2**GGCCTGGGCGGGACTGGGGAG**1**GGT

[a] ONs **3**, **8** and **12** are native unmodified ONs of LTR-III, LTR-IV and LTR-(III + IV), respectively. ONs **4–6** are native LTR-III modified with FBFdU (**1**) and or FdU (**2**) at T_{24} and T_9, respectively. ONs **9** and **10** are native LTR-IV modified with FBFdU (**1**) at T_{12} and T_{19}, respectively. ONs **13–16** are native LTR-(III + IV) modified with FBFdU (**1**) and or FdU (**2**) at T_{25} or T_{32} and T_{10}, respectively. **7** and **11** are complementary ONs of **3** and **8**, respectively.

LTR-III GQ-hairpin motif. Based on the structural considerations, ON **4** was synthesized wherein FBFdU was incorporated at the GQ domain (T_{24}) and FdU was incorporated at the hairpin domain (T_9) using phosphoramidites **1a** and **2a**, respectively (Scheme S1†). The ON was purified by gel electrophoresis and characterized by mass analysis (Fig. S1 and S2, Table S1†). CD spectra of control unmodified ON **3** and modified ON **4** were found to be similar depicting the formation of a hybrid GQ topology with positive bands at ~265 nm and ~285 nm (Fig. S3A†).[14] The GQ form of ON **4** exhibited a slightly higher T_m value as compared to the native ON **3** (Fig. S3B and Table S2†). These results indicate that the incorporation of FBFdU and FdU has only a minor impact on the formation and stability of the ON **4** GQ structure.

The ability of FBFdU to serve as a GQ reporter was evaluated by recording fluorescence of LTR-III ON **4** and its corresponding duplex (**4**·**7**) in a buffer containing K^+ ions (Fig. 2A and B). The GQ form of **4** displayed a discernibly lower fluorescence intensity and a slightly red-shifted emission band (417 nm) as compared to its perfect duplex (**4**·**7**, 414 nm). In support of our probe system design, the ^{19}F NMR spectrum of ON **4** exhibited two distinct peaks at −122.51 ppm and −165.73 ppm arising from FBFdU and FdU, respectively (Fig. 2C, blue line). ^{1}H NMR spectra of ON **4** and **3** revealed imino proton signals for both GQ and hairpin domains (Fig. S4†). To assign signals in the ^{19}F NMR spectrum, two singly modified ONs **5**, containing FBFdU at T_{24} (GQ domain) and **6**, containing FdU at T_9 (hairpin domain), were synthesized (Table 1, Fig. 2A, S1 and S2†). CD profiles and T_m values indicated the formation of a stable hybrid GQ structure like the native **3** and modified **4** ONs (Fig. S3A and B, Table S2†). While ON **5** produced a single peak at −122.51 ppm from the GQ sensor (Fig. 2C, red line), ON **6** gave a signal at −165.71 ppm from the hairpin sensor similar to ON **4** (Fig. 2C, green line). Hence, signals emanating from FBFdU (−122.51 ppm) and FdU (−165.73 ppm) of ON **4** are assigned to GQ and hairpin domains, respectively. When ON **4** was annealed to its complementary ON **7**, the duplex structure produced new peaks at −121.54 ppm associated with FBFdU and −165.62 ppm associated with FdU (Fig. S5†). ^{1}H NMR also validated the formation of a duplex structure where characteristic peaks for Watson–Crick H-bonded imino protons appeared between 12 and 14 ppm, with no peaks in the GQ region (Fig. S5†). Henceforth, the probe system provides a simplified ^{19}F NMR spectrum to detect the two domains of LTR-III ON **4** simultaneously.

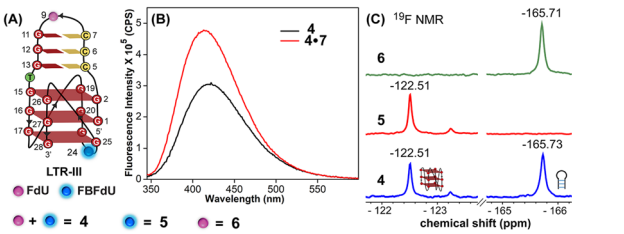

Fig. 2 (A) Schematic representation of the juxtaposed GQ-hairpin structure of LTR-III. ON **4** is modified with FdU at T_9 and FBFdU at T_{24} positions. ON **5** contains FBFdU at the T_{24} position. ON **6** contains FdU at the T_9 position. (B) Fluorescence spectra of ON **4** (GQ) and its duplex **4**·**7**. The samples were excited at 330 nm with excitation and emission slit widths of 7 nm and 9 nm, respectively. (C) ^{19}F NMR spectra of ONs **4–6**.

LTR-IV GQs. Next, we studied the LTR-IV G-rich region by incorporating FBFdU at T_{12} (ON **9**) and T_{19} (ON **10**) positions using the modified phosphoramidite **1a** (Table 1 and Fig. S3A†) and the purity and identity of ONs were ascertained by HPLC and mass analysis (Fig. S1, S2 and Table S1††). According to our presumption, FBFdU placed at these positions did not affect the formation and stability of the native parallel GQ topology as deduced by CD and UV-thermal melting experiments (Fig. S3C and D, Table S2†). ONs **9** and **10** reported the formation of a GQ structure with an intense emission band centered at around 428 nm (Fig. 3B). However, the corresponding duplexes showed reduced emission. In particular, duplex **10**·**11** displayed a significant reduction in fluorescence intensity. Notably, ^{19}F NMR spectra of ON **9** (75 μM) exhibited multiple peaks revealing the formation of different GQ structures (Fig. 3C, blue line). Imino proton signals appearing between 10 and 12 ppm supported the formation of GQs (Fig. S6†). GQs can stack on top of each other by 5′–5′ end-to-end stacking interaction resulting in higher order GQs, and such structures are usually observed for sequences capable of forming a parallel topology.[45] Hence, in consensus with the literature,[15] the observed ^{19}F signals could be associated with higher order structures originating from the monomeric parallel GQ motif. To further evaluate the ^{19}F signals, NMR spectra of ON **9** were recorded at a much lower concentration (favors monomeric form) and in the presence of a synthetic crowding agent (*e.g.*, PEG, favors higher-ordered structures).[46] ^{19}F NMR recorded at a lower concentration of the ON **9** (10 μM) produced a major peak at −120.42 ppm, which was also present at a higher concentration of the ON (Fig. 3C, purple line). While this peak was assigned to the monomeric GQ structure, a peak at −121.74 ppm in PEG 200 (40% v/v) is likely due to the formation of a higher-ordered GQ structure (green line). The formation of GQ structures under these conditions was further confirmed by ^{1}H NMR (Fig. S6†). ON **9** hybridized to its complementary ON **11** exhibited a single ^{19}F peak for the duplex form, which was also ascertained by ^{1}H NMR (Fig. 3C, red line and Fig. S6†). Although ON **10** containing the modification at the T_{19} position exhibited multiple ^{19}F peaks, the spectrum was not well resolved (Fig. S7†). Peak broadening was also observed in the ^{1}H NMR spectrum, and hence, this sequence was not used in further studies. Taken together, these results endorse that FBFdU is a useful GQ tool that allows access to study sequences forming multiple structures.

Probing the GQ structure of the LTR in a physiological environment by NMR

The LTR G-rich promoter region encompassing both LTR-III and IV segments was recently characterized by Richter and Phan groups *in vitro* using ^{1}H NMR. Their results suggest that it largely forms a juxtaposed GQ-hairpin motif like LTR-III.[14] As an important step forward, we decided to use the spectral properties of our nucleoside analogs to systematically determine the GQ structure adopted by the LTR region in a cellular environment and probe its druggable space. In-cell ^{19}F NMR has become a powerful tool to study nucleic acid structures in cellular milieu,[37,47–49] as fluorine is 100% abundant, highly sensitive and importantly, absent in cellular systems (no background signal).[50–55] Furthermore, its signal does not undergo significant line broadening in the heterogeneous cellular environment, which is very severe in the case of a proton signal.[56] To determine ^{19}F signatures of the longer LTR region and survey GQ and hairpin structures, ONs **13–15** labeled with FBFdU in the GQ domain or FdU in the hairpin domain were synthesized (Table 1, Fig. 4A, S1 and S2†). Importantly, the modification position was maintained as in the individual LTR G-rich segments. CD spectra of modified (**13–15**) and control unmodified (**12**) ONs exhibited bands similar to the hybrid topology adopted by the LTR-III region (Fig. S8A†). While ON **13** (FBFdU at T_{25}) displayed a nearly 4 °C higher T_m compared to the native ON **12**, ON **14** (FBFdU at T_{32}) and **15** (FdU at T_{10}) displayed similar T_m values (Fig. S8B and Table S2†). ON **13** showed a single broad ^{19}F peak at −123.20 ppm and ON **14** exhibited a sharper peak at −122.10 ppm for the GQ domain (Fig. 4B). ON **15** produced a distinct peak (−165.72 ppm) for the hairpin domain. ^{1}H NMR spectra of ONs clearly revealed the presence of imino protons for GQ and hairpin motifs (Fig. 4B). Furthermore, the absence of multiple ^{19}F peaks suggests that the parallel topology of the LTR-IV region is possibly not formed by the longer promoter region (compare with Fig. 3C). To detect both GQ and hairpin motifs simultaneously, we synthesized ON

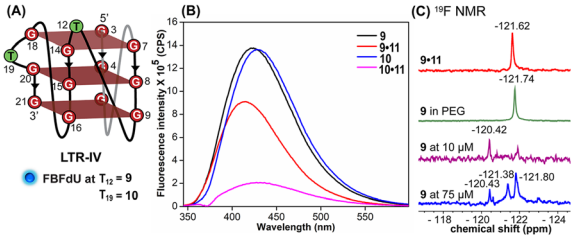

Fig. 3 FBFdU reports the formation of LTR-IV GQs. (A) Schematic representation of the parallel GQ structure of LTR-IV ON. ON **9** contains FBFdU at the T_{12} position. ON **10** contains FBFdU at the T_{19} position. **9**·**11** and **10**·**11** are corresponding duplexes. (B) Fluorescence spectra (1 μM) of ONs **9** and **10** (GQ) and their duplexes. The samples were excited at 330 nm with excitation and emission slit widths of 6 nm and 7 nm, respectively. (C) ^{19}F NMR spectra of ON **9** under different conditions.

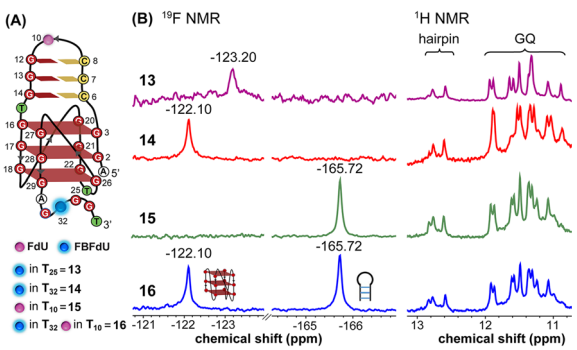

Fig. 4 (A) Schematic representation of the juxtaposed GQ-hairpin structure of the LTR-III + IV region. (B) ^{19}F NMR and partial ^{1}H NMR spectra of ONs **13–16**.

16 containing FdU at T_{10} and FBFdU at T_{32} positions. Modification at T_{25} (like in ON **13**) was avoided as it led to a broader peak and poor base line.

Rewardingly, ON **16** displayed two distinct signals, one each for GQ (−122.10 ppm) and hairpin (−165.72 ppm) structures with the same chemical shifts as that of ONs **14** and **15** designed to detect the structures independently (Fig. 4B). Also, ON **16** depicted a ^{1}H NMR spectrum revealing the presence of GQ and hairpin structures. Collectively, the probe combination provides distinct and simplified ^{19}F signatures for GQ and hairpin structures, and our results demonstrate that the LTR G-rich region predominantly folds into a GQ-hairpin motif similar to LTR-III *in vitro*.

To obtain a progressive understanding of the LTR GQs in cell-free and cellular environments, we performed a systematic NMR analysis using *Xenopus* oocytes, a commonly used cellular model.[47–49,57] While a buffer mimicking intraoocyte (IO) ionic conditions serves as a cell-free system, frog egg lysate and extract serve as very good *ex vivo* systems to carry out NMR experiments to determine the structure of nucleic acids. First, we recorded the ^{19}F NMR spectrum of ON **16** in an IO buffer (25 mM HEPES pH 7.5, 110 mM KCl, 10.5 mM NaCl, 130 nM $CaCl_2$, 1 mM $MgCl_2$, 0.1 mM EDTA). The ON acquired a conformation like LTR-III, reflecting peaks at −122.02 ppm for the GQ and −165.65 ppm for the hairpin motifs (Fig. 5, blue line and Fig. S9†). The formation of the GQ-hairpin structure was confirmed by ^{1}H NMR and CD experiments (Fig. 5 and S10†). ON **16** incubated in the lysate supported the formation of a hybrid architecture like in the IO buffer (Fig. 5, red line). The inter-phase egg extract obtained by simply centrifuging crushed eggs maintains metabolite and protein contents mimicking those in the biological environment.[46] Interestingly, the ^{19}F NMR spectrum of ON **16** incubated in the egg extract revealed the presence of GQ and hairpin motifs, albeit with a slight broadening and shift in the signal (green line). In contrast, due to extensive line broadening, the ^{1}H NMR spectrum fails to provide structural information in egg extract (Fig. 5).[46,57] Therefore, our fluorine-labeled nucleoside probes outweigh the applicability of proton NMR in cell-based analysis. To confirm if the signal is originating from the intact ON in cellular samples, after NMR acquisition, the samples were analyzed by HPLC and ESI-MS. The results indicated that the ON is not degraded in the cellular environment (Fig. S11 and S12†). Taken together, these results provide clear evidence for the presence of a monomeric architecture preserving juxtaposed GQ and hairpin domains both *in vitro* and under cellular conditions underscoring the potential of LTR GQ as a target of selective therapeutic intervention.

Computational models provide insights on how the probe system senses LTR GQs. Fluorescence of FBFdU is enhanced and red-shifted in a polar environment but quenched by stacking interaction and the electron transfer process with an adjacent guanosine base (Table S3†).[37,58] Also, the orientation of the FBF ring relative to uracil impacts its fluorescence intensity. Therefore, observed differences in fluorescence intensity of GQ and duplex structures are due to differences in the microenvironment around the probe. To examine the probe environment and its interaction with neighboring bases, structural models of labeled LTR-III ON **4** and LTR-IV ONs **9** and **10** were generated. Force field parameters of FdU and FBFdU (Fig. S13 and S14†) were first calculated and were incorporated into the templates with PDB ID: 6H1K and 2N4Y.[14,15] Two control systems, LTR-III ON **3** and LTR-IV ON **8**, were also generated. The root mean square deviation (RMSD) revealed that MD simulations are well equilibrated (Fig. S15†). Superimposition of the major cluster of ON **4** and the native ON **3** is almost identical (Fig. S16 and Fig. S17A†). In ON **4**, FBFdU placed at T_{24} strongly stacks below the tetrad formed by $G_{25}\cdot G_{28}\cdot G_{17}\cdot G_{21}$ and experiences a hydrophobic environment (Fig. 6A–C). The plots representing the center of mass (COM) distance and angle defined between the normal to FBFdU and G_{28} showed steady values of ∼5 Å and 0–45° (∼82% stacking), respectively, which are the defined parameters for proper stacking interaction (Fig. S18†).[59] This major conformation exists for ∼86% of the simulation, which manifests in the form of a low intense band around an emission maximum of methanol (417 nm, Fig. 2B). In the case of duplex **4**·**7**, C5-modified FBFdU flanked between C_{23} and G_{25} would be projected in the major groove and is likely to experience less stacking interaction as compared to in the GQ structure. Hence,

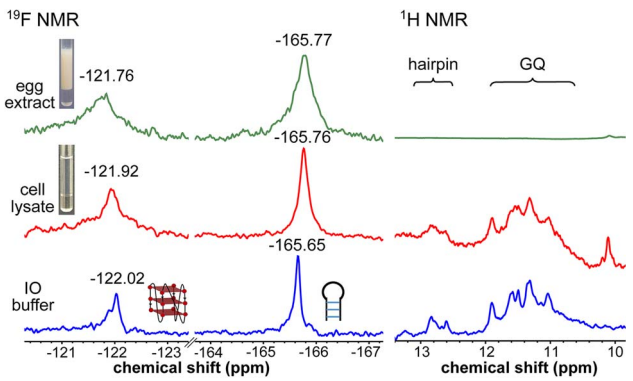

Fig. 5 LTR region forms a GQ-hairpin structure in a cellular environment as detected using FBFdU and FdU. ^{19}F and ^{1}H NMR spectra of ON **16** (100 μM) in IO buffer, frog egg lysate and extract (*ex vivo* cell model).

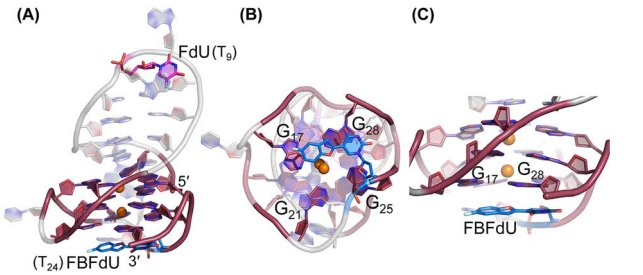

Fig. 6 Representative images of major clusters of LTR-III ON **4**. (A) Overall structure with FdU and FBFdU in ON **4**. (B) Axial view showing the stacking of FBFdU over the bottom quartet. (C) Zoomed-in image showing the perpendicular orientation of FBFdU stacked with G_{17} and G_{28}. GQ bases are represented in maroon, FdU in magenta and FBFdU in blue. K^+ ions are represented as orange spheres. The clusters have been obtained from the 500 ns MD simulation. Details of MD simulations are provided in the ESI.†

the duplex displays higher fluorescence intensity with no apparent change in the emission maximum. A similar conformation has been observed for C5-heterocycle-modified pyrimidine nucleoside analogs in duplexes.[60,61]

Simulations of LTR-IV ON **9** revealed 3 clusters of ~30, 30, and 26% each, and ON **10** revealed 2 clusters accounting for ~85% of the population (Fig. S19 and S20†). The modified base adopts an alternate conformation without affecting the GQ topology (Fig. S21 and S22†). Models of **9** and **10** revealed that the probe placed at T_{12} and T_{19} positions, respectively, is flipped out (solvent exposed) and is away from the G-tetrad core (Fig. S21 and S22†). Hence, these ONs exhibit high fluorescence intensity with emission maxima similar to the emission wavelength of the nucleoside analog **1** in water, indicating a polar environment around the probe (423 nm and 428 nm, Table S3†). In the case of duplex **9**·**11**, FBFdU flanked between C_{11} and G_{13} would experience partial stacking interaction, and hence, shows lower fluorescence intensity at $\lambda_{em} = 418$ nm. FBFdU in duplex **10**·**11** exhibits significant reduction in fluorescence intensity due to partial stacking interaction followed by more quenching from two adjacent Gs (G_{18} and G_{20}). Although the ^{19}F component of nucleoside probes exhibits distinct chemical shifts for different GQ and duplex structures, rationalizing peak positions is not trivial. This is because the environment around the probes and their interaction with neighbouring bases as mentioned above can have varying shielding-deshielding effects on the ^{19}F atom,[62–64] which are difficult to predict and are also evident from an obscure trend in the chemical shift of nucleosides in different solvents (Table S4†).

Probing ligand binding to HIV-1 LTR GQs by fluorescence, ^{19}F NMR and *Taq* DNA polymerase stop assay

Using the spectral properties of the probes, we evaluated ligand recognition of LTR ONs using two structurally different GQ binders namely, TMPyP4 and BRACO19 (Fig. S23A†). Upon ligand binding to the GQ structure, the fluorescence of FBFdU placed in the GQ domain is known to diminish significantly because of its proximity to the polyaromatic ligands.[37] LTR-III ON **4** was titrated with increasing concentrations of the ligands and changes in fluorescence were recorded. Titration with TMPyP4 and BRACO19 resulted in a dose-dependent quenching in fluorescence intensity with minimum changes in the emission maximum (Fig. S24A and B†). A plot of normalized fluorescence intensity *versus* ligand concentration fitted to the Hill equation gave an apparent K_d value of 0.28 ± 0.05 μM and 0.56 ± 0.09 μM, respectively (Fig. S23B†). Similarly the parallel GQ structure of LTR-IV ON **9** titrated with the ligands gave K_d values of 0.33 ± 0.02 μM and 0.39 ± 0.05 μM, respectively (Fig. S23C, S25A and B†). The ^{19}F label of FBFdU efficiently reported the formation of different GQ-ligand complexes with distinct chemical shifts. TMPyP4 and BRACO19 binding to the GQ domain of LTR-III ON **4** produced a new peak at −120.75 ppm and −120.78 ppm, respectively, with a concomitant decrease in the GQ signal (Fig. S23D and S24C†). Gratifyingly, as these ligands bind preferentially to the G-tetrad, they did not exhibit detectable interaction with the hairpin structure. This is evident from the chemical shift of FdU (−165.73 ppm), placed in the hairpin domain, which remains mostly unchanged throughout the titration experiment. Similarly, ligand binding to the parallel topology of LTR-IV ON **9** exhibited a distinct peak for each complex (TMPyP4: −120.77 ppm and BRACO19: −120.60 ppm, Fig. S23E and S25C†). Interestingly, upon ligand binding, multiple GQs formed by **9** coalesce into one ligand-bound form.

Bioinformatics and biophysical studies reveal the prevalence of quadruplex-hairpin/duplex junctions in genomes, characterized by varying loop sizes and conformations.[65–69] These adjacently placed structures offer unique scaffolds to target the junction or both GQ and duplex elements simultaneously.[70–72] Hence, bimodal ligands capable of doing the same can significantly enhance the specific targeting of hybrid GQs as opposed to autonomous GQ structures. In this direction, we evaluated the recognition properties of the GQ-hairpin motif of the longer LTR promoter ON **16** using TMPyP4 (GQ binder) and doxorubicin (DOX, duplex binder) by fluorescence and ^{19}F NMR (Fig. S26A†). Addition of increasing concentrations of TMPyP4 (30 nM–2.5 μM) to ON **16** (0.5 μM) resulted in a progressive quenching in fluorescence intensity as before and gave an apparent K_d value of 0.52 ± 0.03 μM for the formation of the ligand-GQ complex (Fig. S26B and S27A†). Preferential binding of the ligand to the GQ region was ascertained by ^{19}F NMR. FBFdU placed at the GQ domain responded to increasing concentrations of the ligand, giving rise to a new peak at −120.69 ppm for the complex (Fig. 7A). Notably, the chemical shift of FdU (−165.72 ppm) placed in the hairpin domain remained practically unaltered, indicating that TMPyP4 interacts specifically with the GQ structure.

DOX is intrinsically fluorescent and it shows changes in fluorescence upon binding to DNA. To avoid interference from FBFdU, DOX (2 μM) was titrated with a control unmodified ON **12** (2.5 nM–2 μM). We observed a sigmoidal quenching behavior, which gave a K_d value of 0.10 ± 0.02 μM (Fig. 26B and S27B†). ^{19}F NMR using ON **16** gave better insights into the recognition process. Addition of DOX (1 equiv.) to the ON resulted in the emergence of two new peaks–(i) −120.79 ppm associated with GQ-DOX and (ii) −165.98 ppm associated with hairpin-DOX (Fig. 7B). Notably, at a higher equivalent of DOX, the ligand largely occupies the hairpin domain and to some

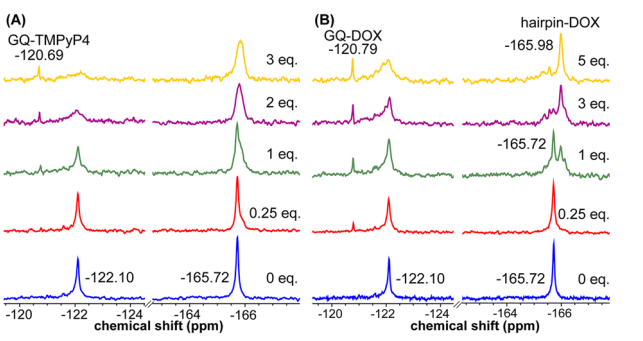

Fig. 7 FBFdU and FdU report structure-specific ligand binding to the LTR GQ-hairpin structure. (A) and (B) ^{19}F NMR spectra of ON **16** as a function of increasing TMPyP4 and DOX concentration, respectively.

extent the GQ domain. These results highlight the advantage of ^{19}F-labeled nucleoside analogs in probing structure-specific ligand interactions. Based on these observations, we designed a polymerase stop assay to study the inhibitory effect of the GQ structure and the ligands independently and in a combination.

The effect of GQ structures on DNA polymerase activity was evaluated by *Taq* DNA polymerase stop assay using a native LTR template **T1** encompassing III and IV regions and a mutated template **T2** (does not fold into a GQ, Fig. 8A and Table S5†). GQ forming template **T1** significantly halted the polymerization process yielding largely stalled products near the GQ site (Fig. S28,† lanes 2–6, 8B). Longer reaction times (30 min) produced only ~33% of the full-length product. In contrast, reactions in the presence of a non-GQ forming template **T2** produced significant amounts of the full-length product in only 2 min (~45%), which progressively increased to ~80% at 30 min (Fig. S28,† lanes 7–11, 8B). These observations indicate that the stalling of the primer extension reaction is due to the formation of a stable LTR GQ structure by **T1**.

Next, we studied the effect of ligand binding to the GQ structure on the polymerase activity using **T1** (Fig. 8C). For this purpose, a reaction time of 20 min was chosen as it gave reasonable amounts of the full-length product (~25%, Fig. S28,† lane 5). Varying concentrations of TMPyP4 and DOX were independently added and allowed to bind with LTR GQ, and then primer extension reactions were carried out as before. Upon addition of TMPyP4 there was a noticeable decrease in the formation of the full-length product, accompanied by a simultaneous increase in stalled products (Fig. S29,† lanes 2–5, Fig. 8D). At 0.75 μM of the ligand (7.5 equiv. w.r.t **T1**) no detectable full-length product was observed (Fig. S29,† lane 6). Similarly, increasing amounts of DOX resulted in a progressive reduction in the formation of the full-length product (Fig. S29,† lane 7–10, Fig. 8D). Although DOX inhibited the polymerase activity, it required a higher amount (20 equiv.) to produce an effect comparable to TMPyP4 (Fig. S29,† compare lane 6 and 10). This may be due to DOX competing for the primer-template duplex, hairpin and GQ regions. These results prompted us to study the combined effect of ligands, wherein different concentrations of TMPyP4 and DOX at a 1 : 1 ratio were added to the reaction mixture. The gel image revealed a synergistic effect of ligands as the formation of the full-length product considerably decreased with a concomitant increase in truncated products in comparison to reactions in which only one ligand was added at an equivalent concentration (Fig. 8D, S29,† lanes 11–14). The effect is noticeable when we compare TMPyP4 (0.3 μM, ~16%), DOX (1 μM, ~17%), and TMPyP4+DOX (0.3 μM, ~9%, Fig. 8D). These results suggest that the GQ-hairpin motif of the LTR G-rich region serves as a highly conserved regulatory element to potentially block the viral replication process by targeting both GQ and hairpin domains simultaneously.

Based on our results and the formation of a unique GQ-hairpin architecture in a cellular environment, we propose that bimodal ligand scaffolds composed of GQ and duplex binders, clamped using an appropriate linker, could selectively target the HIV-1 LTR and profoundly attenuate its pathogenesis (Fig. S30†). Needless to say, careful consideration should be exercised when optimizing the ligand design. The choice of GQ and hairpin binders from available examples and linker length, flexibility and point of attachment to the ligands will be very crucial.

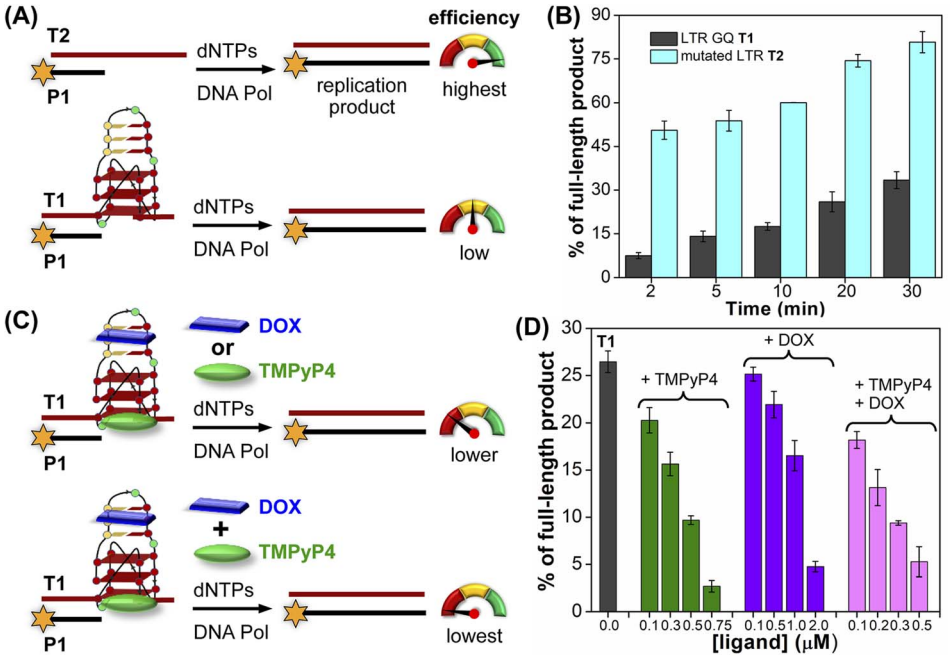

Fig. 8 Schematic representation of primer extension reactions using *Taq* DNA polymerase (A) with non-GQ forming template **T2** and GQ forming template **T1**, (C) in the presence of ligands TMPyP4 or DOX and TMPyP4 + DOX. (B) and (D) Percentage of the full-length product obtained from *Taq* DNA polymerase reactions. (B) Reactions performed using templates **T1** and **T2** at different time intervals. (D) Reactions performed using **T1** with increasing concentrations of ligands TMPyP4, DOX and TMPyP4 + DOX at 20 min. For gel images, see Fig. S28 and S29.† Values are denoted as mean ± s.d for 2 independent experiments.

Conclusion

We have devised a probe platform using two highly environment-sensitive nucleoside analogs (FBFdU and FdU) to study the structural polymorphism of a conserved HIV-1 LTR G-rich region in cell-free and cellular environments. These minimally invasive analogs produced a very simplified spectrum with distinct fluorescence and ^{19}F NMR signatures for different LTR GQ architectures. Importantly, using ^{19}F signatures of FBFdU and FdU we successfully identified that the LTR G-rich region adopts a GQ-hairpin architecture in a cellular environment. MD simulations gave insights on the structural basis by which FBFdU fluorescently senses different GQ topologies and distinguishes them from the duplex form. Furthermore, the nucleoside probes facilitated the detection and estimation of structure-specific ligand interactions by fluorescence and ^{19}F NMR techniques. Polymerase stop assay confirmed the regulatory function of LTR GQ structures. While TMPyP4 (GQ binder) and DOX (duplex binder) individually decreased polymerase activity, an equimolar mixture exhibited a synergistic inhibitory effect on LTR replication. Taken together, these findings suggest that simultaneous targeting of the juxtaposed GQ-hairpin motif using bimodal ligands could be a rational plan to selectively and efficiently inhibit the pathogenesis of the virus. In this direction, the FBFdU and FdU combination offers a versatile platform to study the structure as well as devise screening assays to identify hybrid ligands targeting GQ-hairpin/duplex motifs.

Data availability

The datasets supporting this article have been uploaded as part of the ESI.† Deposited MD simulation models are available in **https://www.modelarchive.org/**. Details are provided in the ESI (Fig. S16, S19 and S20).†

Author contributions

S. G. S. designed and supervised this project. S. R. designed and performed the experiments. P. M., S. S. and P. I. P. performed MD simulations to build models of labeled GQ structures. S. M. and J. K. helped in performing experiments in frog egg lysate and extract. All authors analysed the results, and S. R. and S. G. S. wrote the manuscript in consultation with all the authors.

Conflicts of interest

There are no conflicts to declare.

Acknowledgements

S. R. and S. M. acknowledge CSIR, India, for their graduate research fellowships. P. M. thanks IIT Bombay and S. S. thanks Prime Ministers Research Fellowship (PMRF) for graduate research fellowships. We thank Spacetime-IIT Bombay for HPC facilities. This work was supported by SERB (CRG/2022/000284) grant to S. G. S and IIT Bombay-Institute of Eminence (IOE) funds to P. I. P.

References

1 Y. Peng, Y. Zong, D. Wang, J. Chen, Z.-S. Chen, F. Peng and Z. Liu, *Front. Pharmacol*, 2023, **26**, 1294966.
2 R. J. Pomerantz, *Clin. Infect. Dis.*, 2002, **34**, 91–97.
3 R. K. Gupta, J. Gregson, N. Parkin, H. Haile-Selassie, A. Tanuri, F. L. Andrade, P. Kaleebu, C. Watera, A. Aghokeng, N. Mutenda, J. Dzangare, S. Hone, Z. Z. Hang, J. Garcia, Z. Garcia, P. Marchorro, E. Beteta, A. Giron, R. Hamers, S. Inzaule, L. M. Frenkel, M. H. Chung, T. de Oliveira, D. Pillay, K. Naidoo, A. Kharsany, R. Kugathasan, T. Cutino, G. Hunt, S. A. Rios, M. Doherty, M. R. Jordan and S. Bertagnolio, *Lancet Infect. Dis.*, 2018, **18**, 346–355.
4 A. Archin, L. Liberty, A. D. Kashuba, S. K. Choudhary, J. D. Kuruc, A. M. Crooks, D. C. Parker, E. M. Anderson, M. F. Kearney, M. C. Strain, D. D. Richman, M. G. Hudgens, R. J. Bosch, J. M. Coffin, J. J Eron, D. J. Hazuda and D. M. Margolis, *Nature*, 2012, **487**, 482–485.
5 W. Nguyen, J. Jacobson, K. E. Jarman, H. Jousset Sabroux, L. Harty, J. McMahon, S. R. Lewin, D. F. Purcell and B. E. Sleebs, *J. Med. Chem.*, 2019, **62**, 5148–5175.
6 J. Zhang and C. Crumpacker, *Viruses*, 2022, **14**, 1084.
7 K. A. Roebuck and M. Saifuddin, *Gene Expression*, 1999, **8**, 67–84.
8 T. van Opijnen, R. E. Jeeninga, M. C Boerlijst, G. P. Pollakis, V. Zetterberg, M. Salminen and B. Berkhout, *J. Virol.*, 2004, **78**, 3675–3683.
9 L. A. Pereira, K. Bentley, A. Peeters, M. J. Churchill and N. J. Deacon, *Nucleic Acids Res.*, 2000, **28**, 663–668.
10 R. E. Jeeninga, M. Hoogenkamp, M. Armand-Ugon, M. de Baar, K. Verhoef and B. Berkhout, *J. Virol.*, 2000, **74**, 3740–3751.
11 R. Perrone, M. Nadai, I. Frasson, J. A. Poe, E. Butovskaya, T. E. Smithgall, M. Palumbo, G. Palu and S. N. Richter, *J. Med. Chem.*, 2013, **56**, 6521–6530.
12 S. Amrane, A. Kerkour, A. Bedrat, B. Vialet, M.-L. Andreola and J.-L. Mergny, *J. Am. Chem. Soc.*, 2014, **136**, 5249–5252.
13 A. De Rache, J. Marquevielle, S. Bouaziz, B. Vialet, M. L. Andreola, J.-L. Mergny and S. Amrane, *J. Mol. Biol.*, 2023, **436**, 168359.
14 E. Butovskaya, B. Heddi, B. Bakalar, S. N. Richter and A. T. Phan, *J. Am. Chem. Soc.*, 2018, **140**, 13654–13662.
15 B. De Nicola, C. J. Lech, B. Heddi, S. Regmi, I. Frasson, R. Perrone, S. N. Richter and A. T. Phan, *Nucleic Acids Res.*, 2016, **44**, 6442–6451.
16 E. Ruggiero, I. Frasson, E. Tosoni, M. Scalabrin, R. Perrone, M. Marušič, J. Plavec and S. N. Richter, *ACS Infect. Dis.*, 2022, **8**, 958–968.
17 Y. Sheng, B. Cao, M. X. Ou, Y. Wang, S. M. Yuan, N. Zhang, T. Zou and Y. Liu, *Chem. Commun.*, 2021, **57**, 5298–5301.
18 R. Perrone, E. Lavezzo, G. Palù and S. N. Richter, *Sci. Rep.*, 2017, **7**, 2018.
19 M. Vorlíčková, I. Kejnovská, J. Sagi, D. Renčiuk, K. Bednářová, J. Motlová and J. Kypr, *Methods*, 2012, **57**, 64–75.

20 R. A. Darby, M. Sollogoub, C. McKeen, L. Brown, A. Risitano, N. Brown, C. Barton, T. Brown and K. R. Fox, *Nucleic Acids Res.*, 2002, **30**, e39.
21 B. R. Vummidi, J. Alzeer and N. W. Luedtke, *ChemBioChem*, 2013, **14**, 540–558.
22 J. Mohanty, N. Barooah, V. Dhamodharan, S. Harikrishna, P. I Pradeepkumar and A. C. Bhasikuttan, *J. Am. Chem. Soc.*, 2013, **135**, 367–376.
23 D. Sun and L. H. Hurley, *Methods Mol. Biol.*, 2010, **608**, 65–79.
24 S. M. Haider, G. N. Parkinson and S. Neidle, *J. Mol. Biol.*, 2003, **326**, 117–125.
25 T. Santos, G. F. Salgado, E. J. Cabrita and C. S. Cruz, *Pharmaceuticals*, 2021, **14**, 769.
26 G. Biffi, D. Tannahill, J. McCafferty and S. Balasubramanian, *Nat. Chem.*, 2013, **5**, 182–186.
27 A. Henderson, Y. Wu, Y. C. Huang, E. A. Chavez, J. Platt, F. B. Johnson, R. M. Brosh Jr, D. Sen and P. M. Lansdrop, *Nucleic Acids Res.*, 2014, **42**, 860–869.
28 S. Galli, L. Melidis, S. M. Flynn, D. Varshney, A. Simeone, J. Spiegel, S. K. Madden, D. Tannahill and S. Balasubramanian, *J. Am. Chem. Soc.*, 2022, **144**, 23096–23103.
29 F. Doria, M. Nadai, M. Zuffo, R. Perrone, M. Freccero and S. N. Richter, *Chem. Commun.*, 2017, **53**, 2268–2271.
30 J. Robinson, S. G. Stenspil, K. Maleckaite, M. Bartlett, M. D. Antonio, R. Vilar and M. K. Kuimova, *J. Am. Chem. Soc.*, 2024, **146**, 1009–1018.
31 J.-H. Yuan, W. Shao, S.-B. Chen, Z.-S. Huang and J.-H. Tan, *Biochem. Biophys. Res. Commun.*, 2020, **531**, 18–24.
32 T. Vo, S. Oxenford, R. Angell, C. Marchetti, S. A. Ohnmacht, W. D. Wilson and S. Neidle, *ACS Med. Chem. Lett.*, 2020, **11**, 991–999.
33 S. Kumar, S. P. P. Pany, S. Sudhakar, S. B. Singh, C. S. Todankar and P. I. Pradeepkumar, *Biochemistry*, 2022, **61**, 2546–2559.
34 S. Takahashi, A. Kotar, H. Tateishi-Karimata, S. Bhowmik, Z. F. Wang, T. C. Chang, S. Sato, S. Takenaka, J. Plavec and N. Sugimoto, *J. Am. Chem. Soc.*, 2021, **143**, 16458–16469.
35 R. Rigo, E. Groaz and C. Sissi, *Pharmaceuticals*, 2022, **15**, 373.
36 J. T. Grün and H. Schwalbe, *Biopolymers*, 2022, **113**, e23477.
37 S. Manna, D. Sarkar and S. G. Srivatsan, *J. Am. Chem. Soc.*, 2018, **140**, 12622–12633.
38 A. Nuthanakanti, I. Ahmed, S. Y. Khatik, K. Saikrishnan and S. G. Srivatsan, *Nucleic Acids Res.*, 2019, **47**, 6059–6072.
39 M. Cheng, Yu. Cheng, J. Hao, G. Jia, J. Zhou, J.-L. Mergny and C. Li, *Nucleic Acids Res.*, 2018, **46**, 9264–9275.
40 J. Jana, Y. M. Vianney, N. Schröder and K. Weisz, *Nucleic Acids Res.*, 2022, **50**, 7161–7175.
41 M. Sproviero, K. L. Fadock, A. A. Witham and R. A. Manderville, *ACS Chem. Biol.*, 2015, **10**, 1311–1318.
42 S. Manna and S. G. Srivatsan, *RSC Adv.*, 2018, **8**, 25673–25694.
43 M. Olejniczak, Z. Gdaniec, A. Fischer, T. Grabarkiewicz, L. Bielecki and R. W. Adamiak, *Nucleic Acids Res.*, 2002, **30**, 4241–4249.
44 K. Tanabe, M. Sugiura and S. Nishimoto, *Bioorg. Med. Chem.*, 2010, **18**, 6690–6694.
45 N. Q. Do and A. T. Phan, *Chem.–Eur. J.*, 2012, **18**, 14752–14759.
46 R. Hänsel, F. Löhr, S. Foldynová-Trantírková, E. Bamberg, L. Trantírek and V. Dötsch, *Nucleic Acids Res.*, 2011, **39**, 5768–5775.
47 H.-L. Bao, T. Ishizuka, T. Sakamoto, K. Fujimoto, T. Uechi, N. Kenmochi and Y. Xu, *Nucleic Acids Res.*, 2017, **45**, 5501–5511.
48 H.-L. Bao, T. Masuzawa, T. Oyoshi and Y. Xu, *Nucleic Acids Res.*, 2020, **48**, 7041–7051.
49 C. Wang, G. Xu, X. Liu, L. Jiang, X. Zhou, M. Liu and C. Li, *J. Am. Chem. Soc.*, 2024, **146**, 4741–4751.
50 H. Chen, S. Viel, F. Ziarelli and L. Peng, *Chem. Soc. Rev.*, 2013, **42**, 7971–7982.
51 D. Gimenez, A. Phelan, C. D. Murphy and S. L. Cobb, *Beilstein J. Org. Chem.*, 2021, **17**, 293–318.
52 K. Fauster, C. Kreutz and R. Micura, *Angew. Chem., Int. Ed.*, 2012, **51**, 13080–13084.
53 M. R. Baranowski, M. Warminski, J. Jemielity and J. Kowalska, *Nucleic Acids Res.*, 2020, **48**, 8209–8224.
54 Q. Li, M. Trajkovski, C. Fan, J. Chen, Y. Zhou, K. Lu, H. Li, X. Su, Z. Xi, J. Plavec and C. Zhou, *Angew. Chem., Int. Ed.*, 2022, **61**, e2022018.
55 M. Wang, M. Lu, M. P. Fritz, C. M. Quinn, I. L. Byeon, C.-H. Byeon, J. Struppe, W. Maas, A. M. Gronenborn and T. Polenova, *Angew. Chem., Int. Ed.*, 2018, **57**, 16375–16379.
56 L. B. T. Pham, A. Costantino, L. Barbieri, V. Calderone, E. Luchinat and L. Banci, *J. Am. Chem. Soc.*, 2023, **145**, 1389–1399.
57 R. Hänsel, S. Foldynová-Trantírková, F. Löhr, J. Buck, E. Bongartz, E. Bamberg, H. Schwalbe, V. Dötsch and L. Trantírek, *J. Am. Chem. Soc.*, 2009, **131**, 15761–15768.
58 S. Doose, H. Neuweiler and M. Sauer, *ChemPhysChem*, 2009, **10**, 1389–1398.
59 H. S. Hayatshahi, N. M. Henriksen and T. E. Cheatham, *J. Chem. Theory Comput.*, 2018, **14**, 1456–1470.
60 N. J. Greco and Y. Tor, *J. Am. Chem. Soc.*, 2005, **127**, 10784–10785.
61 J. Riedl, R. Pohl, L. Rulíšek and M. Hocek, *J. Org. Chem.*, 2012, **77**, 1026–1044.
62 H. Sapper and W. Lohmann, *Biophys. Struct. Mech.*, 1978, **4**, 327–335.
63 C. S. Giam and J. L. Lyle, *J. Am. Chem. Soc.*, 1973, **95**, 3235–3239.
64 J. N. Dahanayake, C. Kasireddy, J. P. Karnes, R. Verma, R. M. Steinert, D. Hildebrandt, O. A. Hull, J. M. Ellis and K. R. Mitchell-Koch, *Annu. Rep. NMR Spectrosc.*, 2018, **93**, 281–365.
65 Y. M. Vianney and K. Weisz, *Nucleic Acids Res.*, 2022, **50**, 11948–11964.
66 M. L. Greco, A. Kotar, R. Rigo, C. Cristofari, J. Plavec and C. Sissi, *Nucleic Acids Res.*, 2017, **45**, 10132–10142.
67 M. Yang, S. Carter, S. Parmar, D. D. Bume, D. R. Calabrese, X. Liang, K. Yazdani, M. Xu, Z. Liu, C. J. Thiele and J. S. Schneekloth, *Nucleic Acids Res.*, 2021, **49**, 7856–7869.

68 S. Y. Khatik, S. Sudhakar, S. Mishra, J. Kalia, P. I. Pradeepkumar and S. G. Srivatsan, *Chem. Sci.*, 2023, **14**, 5627–5637.
69 R. K. R. Sannapureddi, M. K. Mohanty, L. Salmon and B. Sathyamoorthy, *J. Am. Chem. Soc.*, 2023, **145**, 15370–15380.
70 L. Díaz-Casado, I. Serrano-Chacón, L. Montalvillo-Jiménez, F. Corzana, A. Bastida, A. G. Santana, C. González and J. L. Asensio, *Chem.–Eur. J.*, 2021, **27**, 6204–6212.
71 T. Q. N. Nguyen, K. W. Lim and A. T. Phan, *Sci. Rep.*, 2017, **7**, 11969.
72 S. Mandal, Y. Kawamoto, Z. Yue, K. Hashiya, Y. Cui, T. Bando, S. Pandey, M. E. Hoque, M. A. Hossain, H. Sugiyama and H. Mao, *Nucleic Acids Res.*, 2019, **47**, 3295–3305.

Electronic Supplementary Information (ESI)

Structural elucidation of HIV-1 G-quadruplexes in cellular environment and their ligand binding using responsive ^{19}F-labeled nucleoside probes

Sarupa Roy,[a] Priyasha Majee,[b] Sruthi Sudhakar,[b] Satyajit Mishra,[c] Jeet Kalia,[c,d] P. I. Pradeepkumar[b*] and Seergazhi G. Srivatsan[a*]

[a]Department of Chemistry, Indian Institute of Science Education and Research (IISER), Pune Dr. Homi Bhabha Road, Pune 411008, India. E-mail: srivatsan@iiserpune.ac.in

[b]Department of Chemistry, Indian Institute of Technology Bombay, Mumbai 400076, India. E-mail: pradeep@chem.iitb.ac.in

[c]Department of Biological Sciences, Indian Institute of Science Education and Research (IISER) Bhopal, Bhopal Bypass Road, Bhauri, Bhopal 462066, India.

[d]Department of Chemistry, Indian Institute of Science Education and Research (IISER) Bhopal, Bhopal Bypass Road, Bhauri, Bhopal 462066, India.

1. Materials: 5-Flurobenzofuran-2'-deoxyuridine (**1**) and phosphoramidite substrates (**1a**) and (**2a**) were synthesised following a reported procedure.[S1-S3] 5-fluoro-2'-deoxyuridine (**2**) was purchased from Carbosynth. Monomers for solid-phase oligonucleotide (ON) synthesis such as *N*-benzoyl-protected dA, *N*-acetyl-protected dC, *N,N*-dimethylformamide-protected dG, and dT phosphoramidite substrates were purchased from ChemGenes, Glen Research and Innovassynth. Solid supports for DNA synthesis were procured from Glen Research. All other reagents needed for solid-phase ON synthesis were availed from Sigma-Aldrich. Control DNA ONs **3**, **7**, **8**, **11** and **12** were purchased from Integrated DNA Technology, purified by denaturing polyacrylamide gel electrophoresis (PAGE) and desalted using Sep-Pak Classic C18 cartridges (Waters Corporation). BRACO19 hydrochloride and all reagents (Bio-Ultra grade) used in the preparation of buffers were purchased from Sigma-Aldrich. TMPyP4 and Doxorubicin hydrochloride (DOX) were procured from Merck-Millipore. Millipore water after autoclaving was used for the preparation of all buffer solutions and in all biophysical studies.

2. Instruments: NMR spectra of small molecules were acquired in Bruker AVANCE III HD ASCEND 400 MHz spectrometer and processed using Mnova software from Mestrelab Research. Mass data was obtained using ESI-MS Waters Synapt G2-Si Mass Spectrometry instrument. Modified DNA ONs were synthesized on a K&A DNA/RNA synthesizer H6. RP-HPLC analysis was performed using Agilent Technologies 1260 Infinity HPLC. Absorption spectra were recorded on a UV-2600 Shimadzu spectrophotometer. Fluorescence of the ONs samples were recorded using a Fluoromax-4 spectrophotometer (Horiba Scientific). UV-thermal melting analysis of the ONs was carried out on Cary 300 Bio UV-Vis spectrophotometer and Cary 3500 multicell UV-Vis spectrophotometer. CD measurements were done on a JASCO J-815 CD spectrometer. NMR spectra of the ONs were acquired on a Bruker AVANCE III HD ASCEND 600 MHz spectrometer equipped with Cryo-Probe (CP2.1 QCl 600S3 H/F-C/N-D-05 Z XT) and processed using Bruker TopSpin Software.

3. Solid-phase DNA synthesis: FBFdU (**1**) and or FdU (**2**) modified DNA ONs **4**–**6**, **9**, **10** and **13**–**16** were synthesized on a 1 µmole scale (1000 Å CPG solid support) with K&A H-6 synthesizer using phosphoramidite substrates. For modified phosphoramidites FBFdU (**1a**) and FdU (**2a**), double coupling of 3 min each was set (total 6 min). After the synthesis, the ONs were cleaved from the solid support using 30% aqueous ammonia and deprotected at 65 °C for 20 h. ONs were purified by denaturing PAGE (18 % or 20% gel) and the product bands were visualized by UV-shadowing. Product bands were excised and ONs were extracted with 4 mL of 0.5 M ammonium acetate buffer in a poly-prep column (Bio-Rad) for 12 h. Desalting was performed using a Waters C-18 cartridge. The purity of ONs was monitored by RP-HPLC (Figure S1). The integrity was verified by ESI-MS (Figure S2).

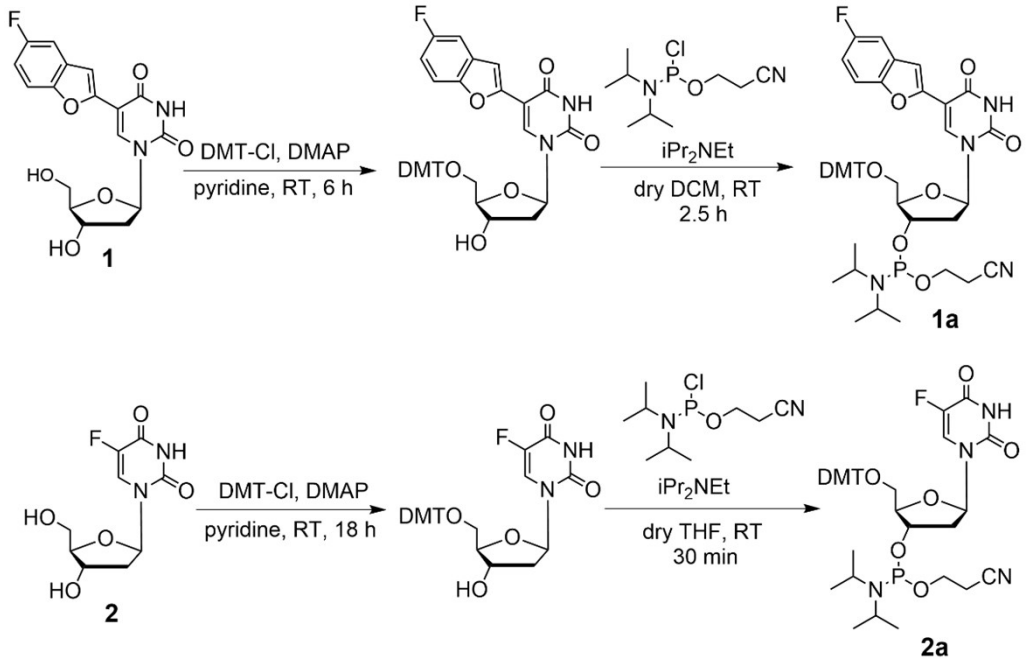

Scheme S1. FBFdU phosphoramidite (**1a**) and FdU phosphoramidite (**2a**) were synthesized following reported procedures.[S1-S3] ^{31}P NMR spectra of phosphoramidites (**1a**) and (**2a**) are enclosed at the end of the ESI.

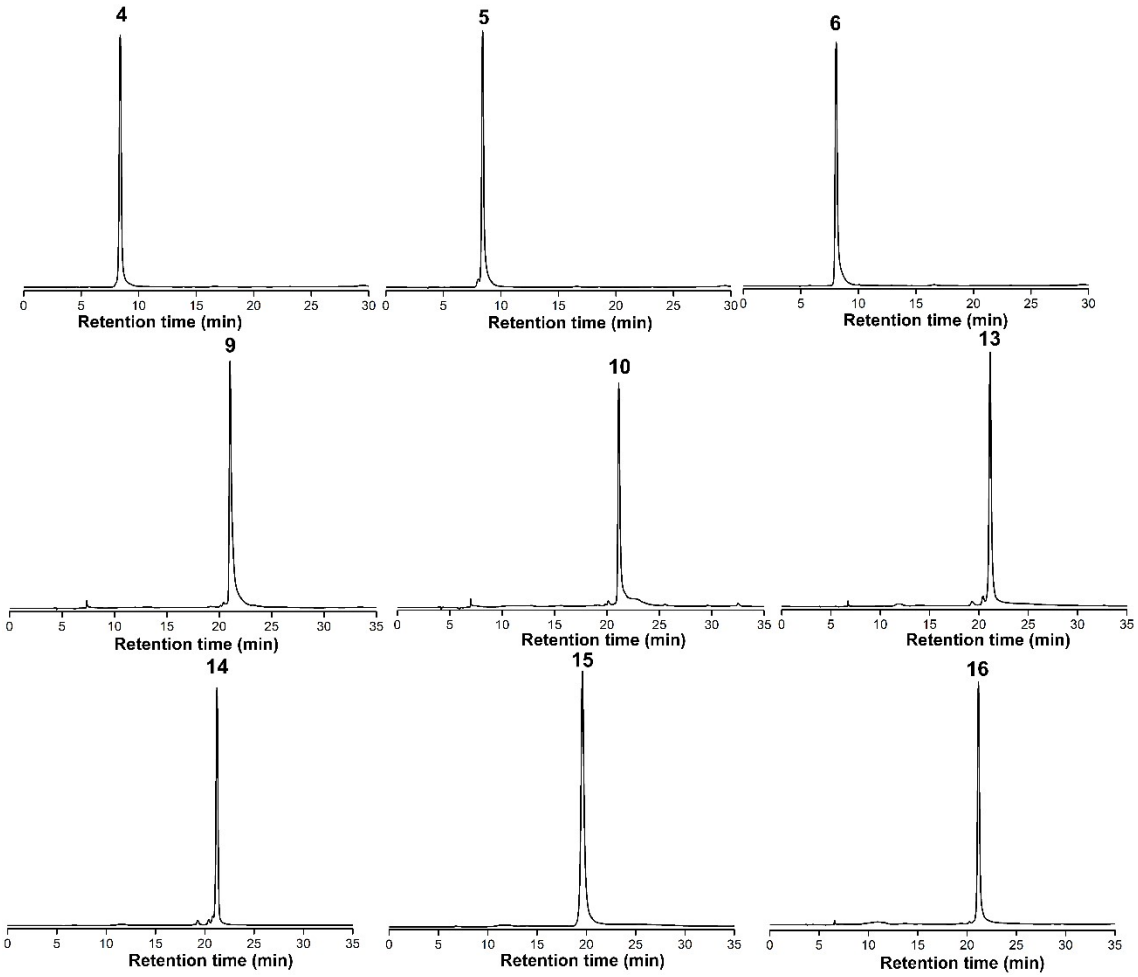

Fig. S1. The purity of PAGE purified ONs containing the modification was analysed by RP-HPLC at 260 nm using Luna C18 column (250 x 4.6 mm, 5 micron). Mobile phase A= 0.5 mM triethylammonium acetate (pH=7.3) and B= acetonitrile. Gradient: 0–100 % B in 30 min with a flow rate of 1 mL/min was used for ONs **4**–**6**. Gradient: 0–30 % B in 40 min and 30–100% in 10 min with a flow rate of 1 mL/min was used for ONs **9**, **10**, **13**–**16**.

4. ESI-MS analysis: Negative mode ESI-MS analysis was performed by injecting DNA ONs (~800 pmol) dissolved in 50% acetonitrile in an aqueous solution of 10 mM triethylamine and 100 mM 1,1,1,3,3,3-hexafluoro-2-propanol. See Figure S2 for mass spectra and Table S1 for details.

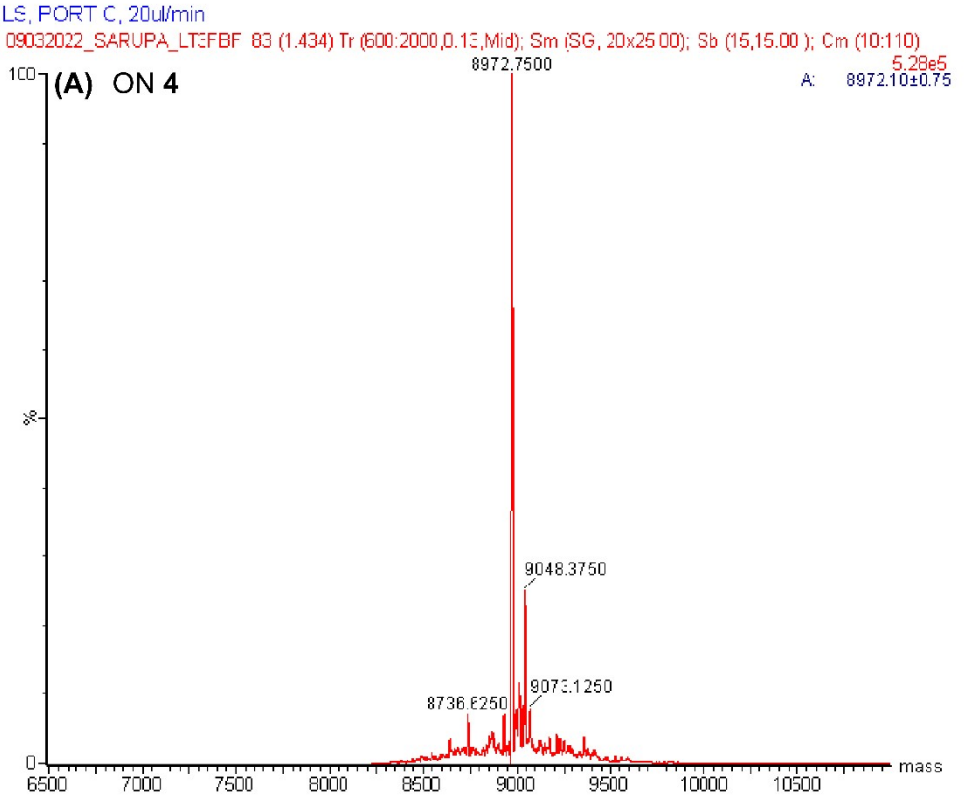
LS, PORT C, 20ul/min
09032022_SARUPA_LTEFBF 83 (1.434) Tr (600:2000,0.13,Mid); Sm (SG, 20x25.00); Sb (15,15.00); Cm (10:110)
(A) ON 4
8972.7500
5.28e5
A: 8972.10±0.75
9048.3750
8736.6250
9073.1250
%
mass
6500
7000
7500
8000
8500
9000
9500
10000
10500

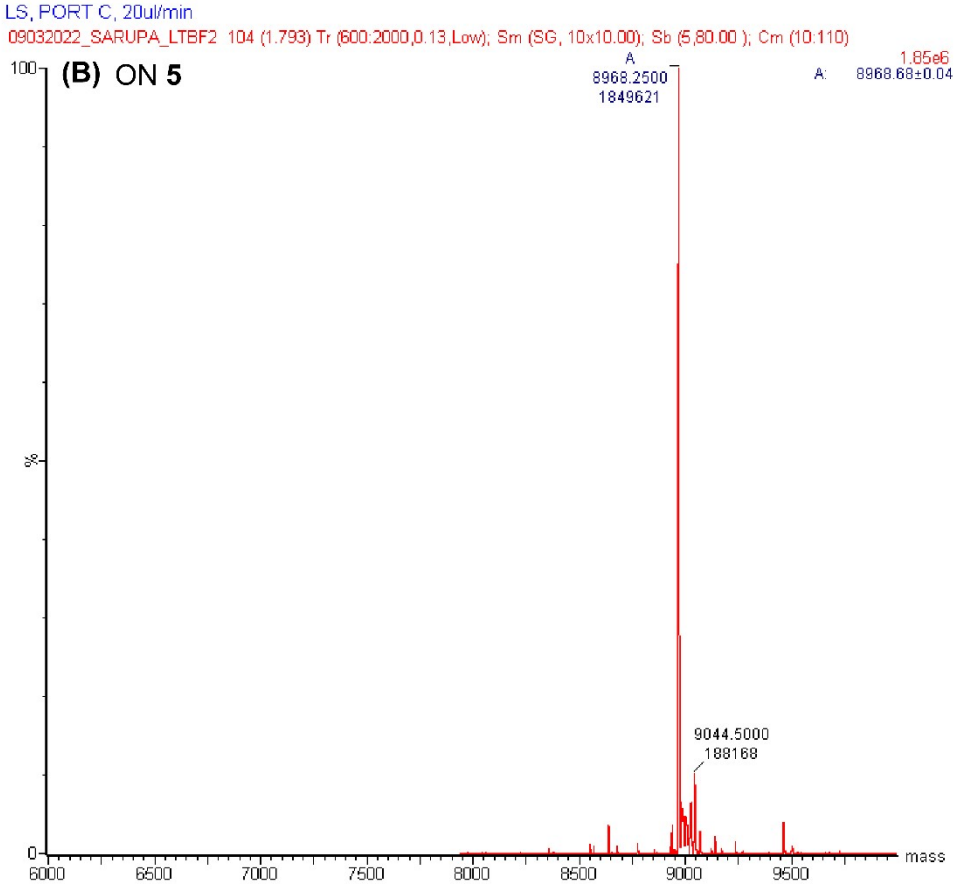
LS, PORT C, 20ul/min
09032022_SARUPA_LTBF2 104 (1.793) Tr (600:2000,0.13,Low); Sm (SG, 10x10.00); Sb (5,80.00); Cm (10:110)
(B) ON 5
A
8968.2500
1849621
1.85e6
A: 8968.68±0.04
9044.5000
188168
%
mass
6000
6500
7000
7500
8000
8500
9000
9500

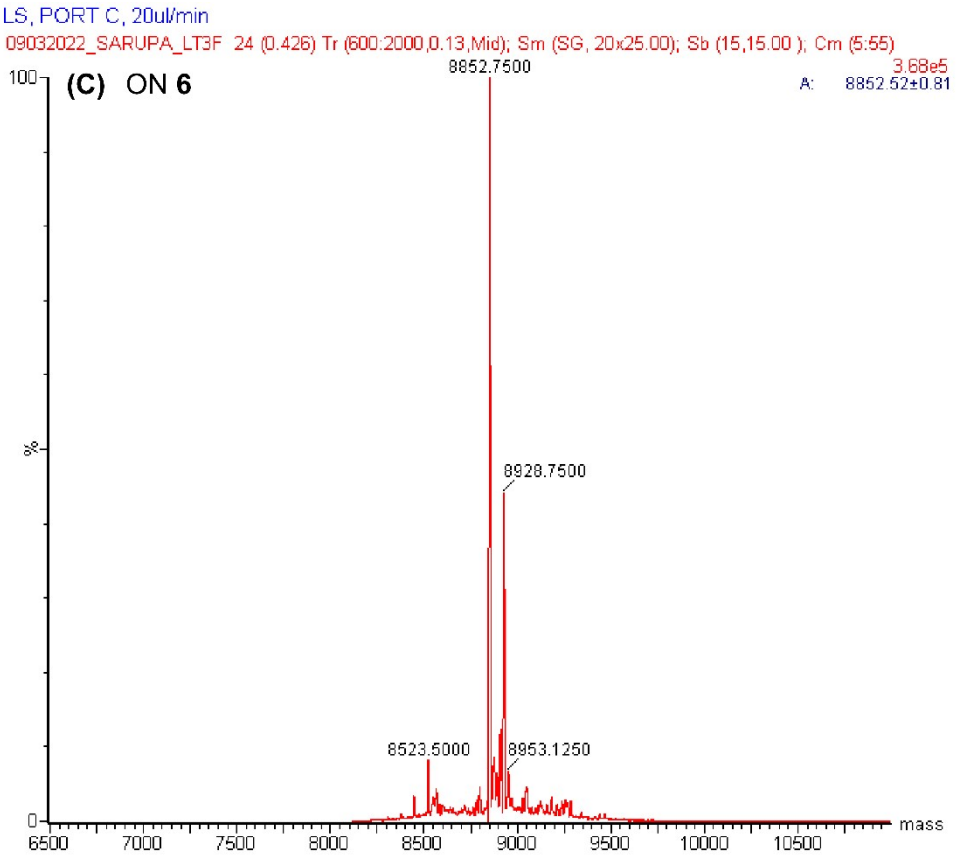
LS, PORT C, 20ul/min
09032022_SARUPA_LT3F 24 (0.426) Tr (600:2000,0.13,Mid); Sm (SG, 20x25.00); Sb (15,15.00); Cm (5:55)
(C) ON 6
3.68e5
A: 8852.52±0.81
8852.7500
8928.7500
8523.5000
8953.1250
100
%
0
6500
7000
7500
8000
8500
9000
9500
10000
10500
mass

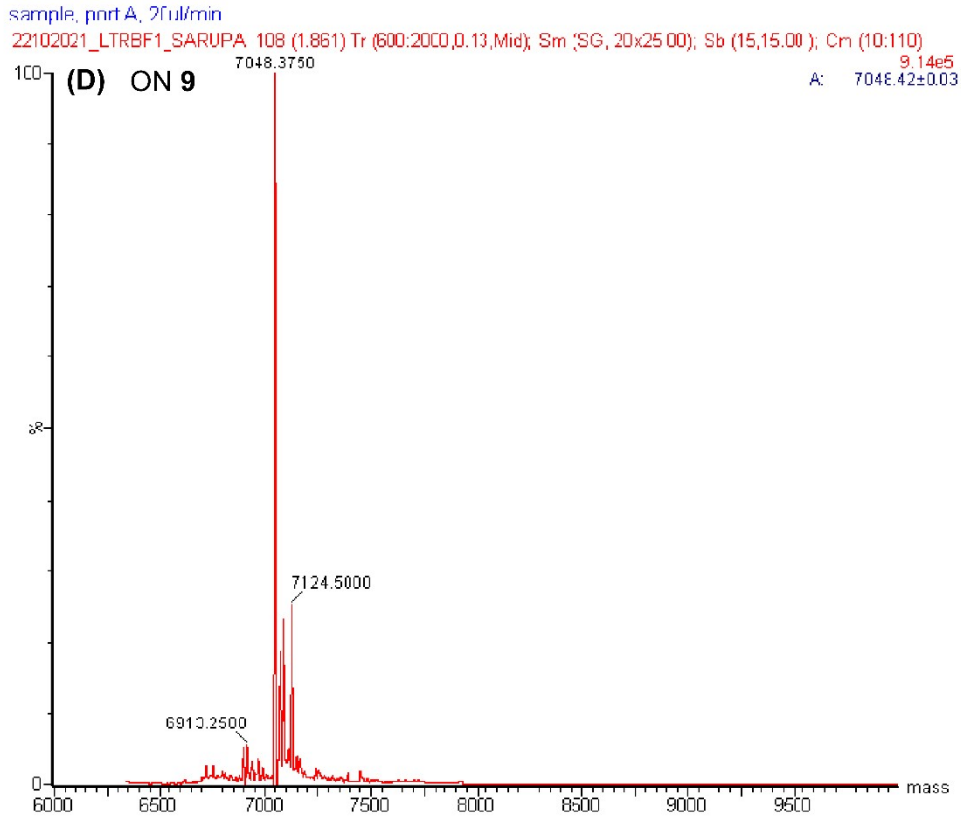
sample, port A, 20ul/min
22102021_LTRBF1_SARUPA 108 (1.861) Tr (600:2000,0.13,Mid); Sm (SG, 20x25.00); Sb (15,15.00); Cm (10:110)
(D) ON 9
9.14e5
A: 7048.42±0.03
7048.3750
7124.5000
6910.2500
100
%
0
6000
6500
7000
7500
8000
8500
9000
9500
mass

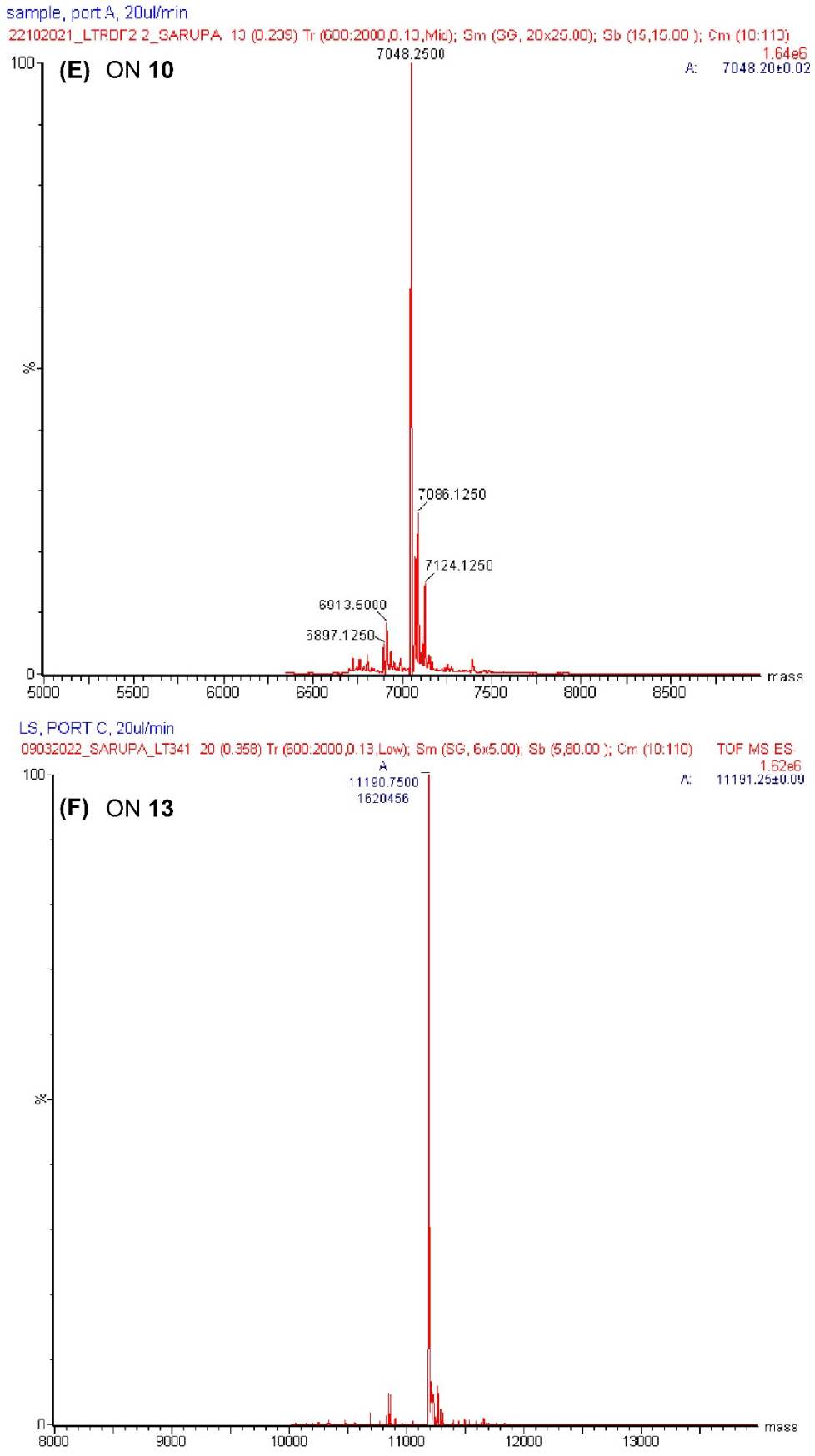
sample, port A, 20ul/min
22102021_LTRDF2 2_SARUPA 10 (0.239) Tr (600:2000,0.10,Mid); Sm (SG, 20x25.00); Sb (15,15.00); Cm (10:110)
(E) ON 10
7048.2500
1.64e6
A: 7048.20±0.02
7086.1250
7124.1250
6913.5000
3897.1250
100
%
0
5000
5500
6000
6500
7000
7500
8000
8500
mass
LS, PORT C, 20ul/min
09032022_SARUPA_LT341 20 (0.358) Tr (600:2000,0.13,Low); Sm (SG, 6x5.00); Sb (5,80.00); Cm (10:110)
TOF MS ES-
A
11190.7500
1620456
1.62e6
A: 11191.25±0.09
(F) ON 13
100
%
0
8000
9000
10000
11000
12000
13000
mass

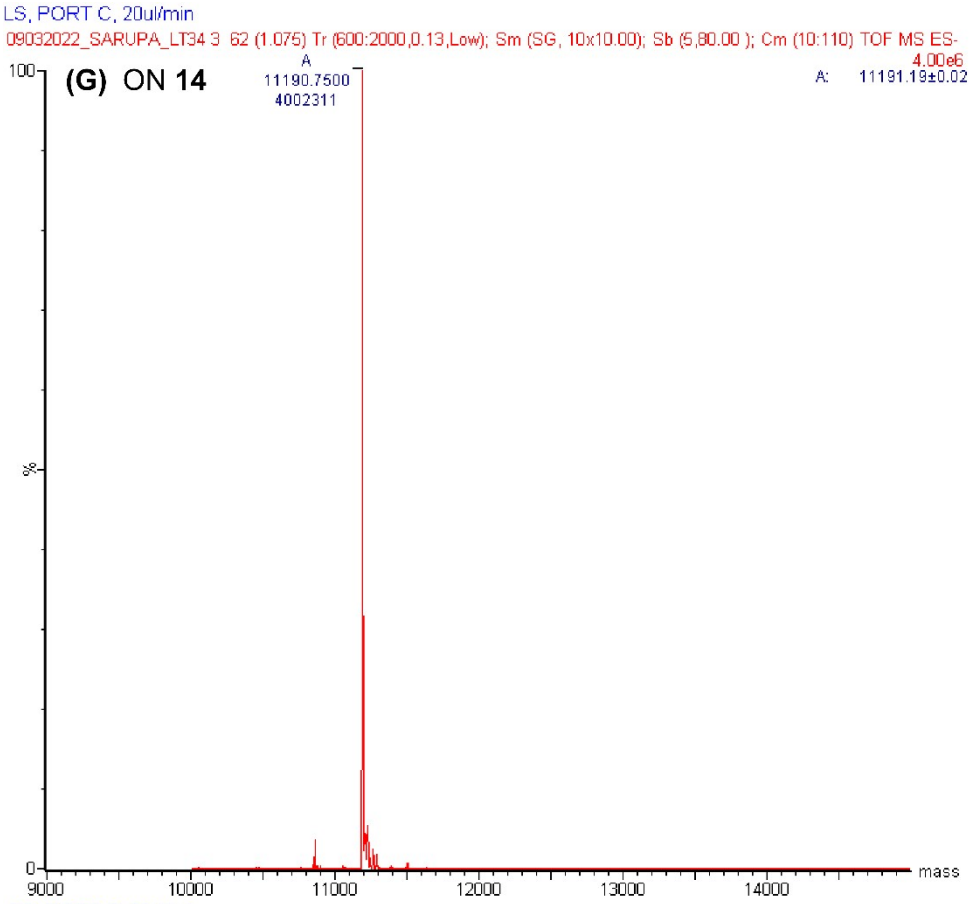
LS, PORT C, 20ul/min
09032022_SARUPA_LT34 3 62 (1.075) Tr (600:2000,0.13,Low); Sm (SG, 10x10.00); Sb (5,80.00); Cm (10:110) TOF MS ES-
4.00e6
(G) ON 14
A
11190.7500
4002311
A: 11191.19±0.02
100
%
0
9000
10000
11000
12000
13000
14000
mass

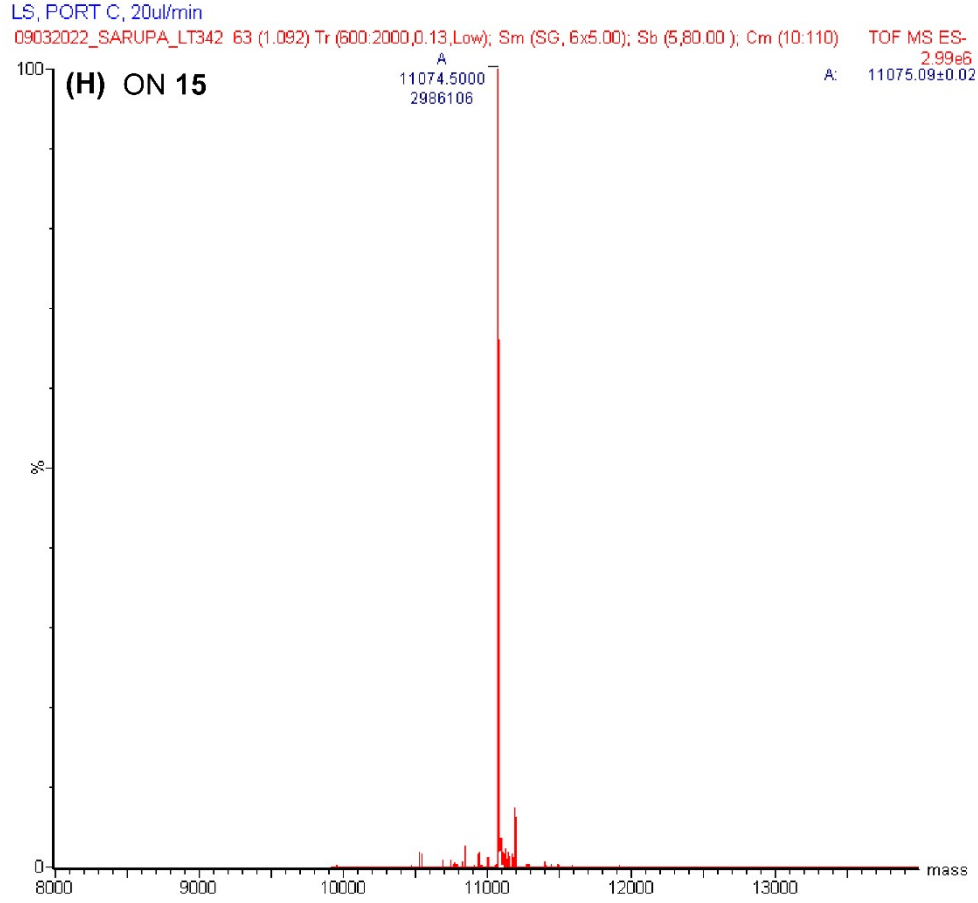
LS, PORT C, 20ul/min
09032022_SARUPA_LT342 63 (1.092) Tr (600:2000,0.13,Low); Sm (SG, 6x5.00); Sb (5,80.00); Cm (10:110)
TOF MS ES-
2.99e6
(H) ON 15
A
11074.5000
2986106
A: 11075.09±0.02
100
%
0
8000
9000
10000
11000
12000
13000
mass

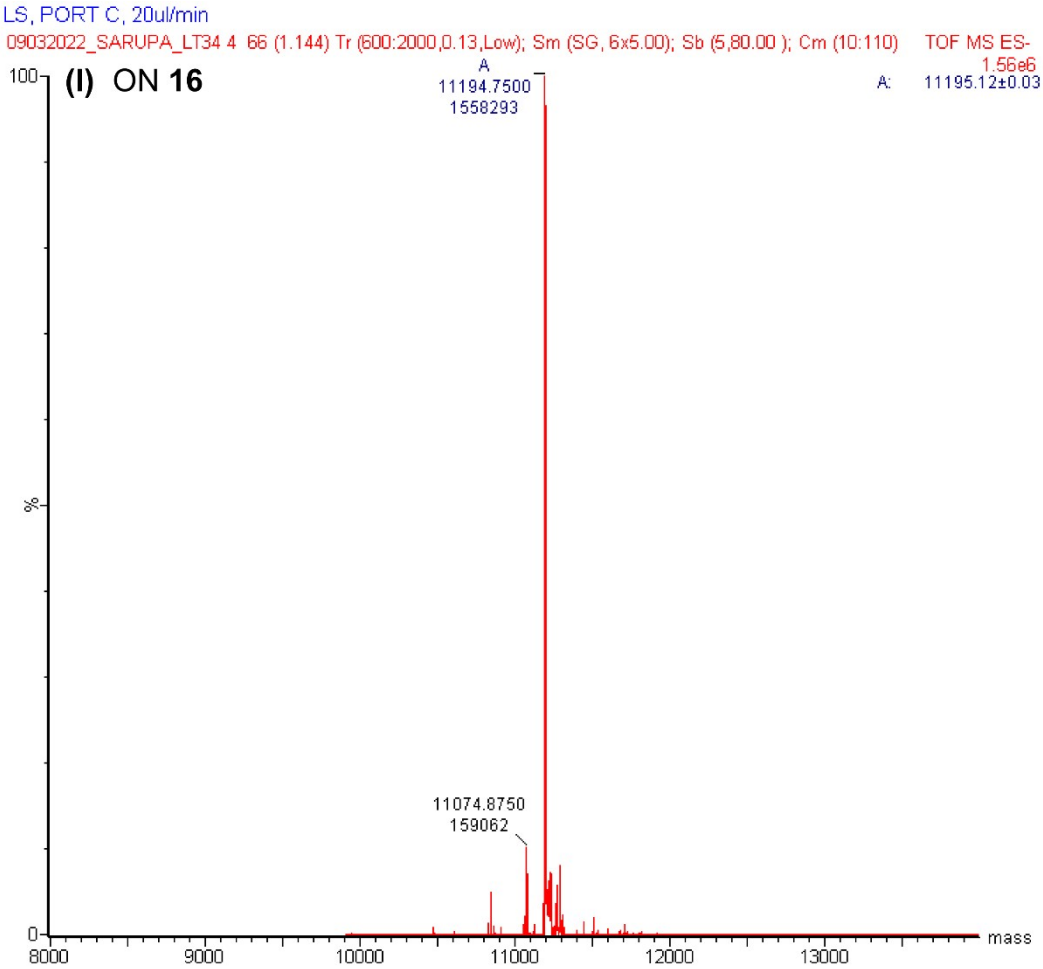

Fig. S2 ESI-MS of purified LTR ONs containing FBFdU and or FdU. See Table S1 for details.

Table S1. ε_{260} and mass data of modified LTR ONs

ON sequence	ε_{260} [M^{-1} cm^{-1}][a]	calculated (g/mol)	found (g/mol)
4	258418	8972.76	8972.75
5	268710	8968.79	8968.25
6	266087	8852.68	8852.75
9	212810	7048.58	7048.37
10	212810	7048.58	7048.25
13	342910	11191.23	11190.75
14	342910	11191.23	11190.75
15	348117	11075.11	11074.50
16	341896	11195.19	11194.75

[a]Molar absorption coefficient (ε) of modified ONs was determined by using OligoAnalyzer 3.1. The molar absorptivity of modified nucleosides FBFdU (ε_{260}= 10310 M^{-1} cm^{-1}) and FdU (ε_{260}= 7687 M^{-1} cm^{-1}) was used in place of dT.

5. Circular dichroism (CD) analysis: ONs **3**–**6**, **8**–**10** and **12**–**16** were annealed in 20 mM potassium phosphate buffer (pH 7) containing 70 mM KCl at 95 °C for 5 min and slowly cooled to RT. CD spectra were recorded from 320–200 nm at 25 °C using 1 nm bandwidth and sample volume of 200 µL using a quartz cuvette (Sterna Scientific, path length 2 mm) on a Jasco J-815 CD spectrometer. Each spectrum was recorded in duplicate with averaging three accumulations at scanning speed of 100 nm/min and baseline corrected for buffer contribution. Each spectrum was smoothened using the software provided by the manufacturer present in the system.

CD analysis in intraoocyte (IO) buffer: Control ON **12** (5 µM) and modified ON **16** (5 µM) were annealed in intraoocyte (IO) buffer (25 mM HEPES (pH 7.5), 10.5 mM NaCl, 110 mM KCl, 130 nM $CaCl_2$, 1 mM $MgCl_2$, 0.1 mM EDTA) at 95 °C for 5 minutes and allowed to cool at RT. CD spectra were recorded as mentioned above.

6. Thermal melting analysis: ONs **3**–**6**, **8**–**10** and **12**–**16** were annealed in 20 mM potassium phosphate buffer (pH 7) containing 70 mM KCl as mentioned above. The spectra were recorded in Cary 300 Bio UV–Vis spectrophotometer for ONs **3**–**6** and ONs **12**–**16**. Cary 3500 multicell UV-Vis spectrophotometer was used for recording the spectra for ONs **8**–**10** with a temperature interval of 1 °C. Absorbance was recorded at 295 nm with a data interval of 1 °C for ONs **3**–**6**, ONs **12**–**16** and 0.5 °C for ONs **8**–**10**.

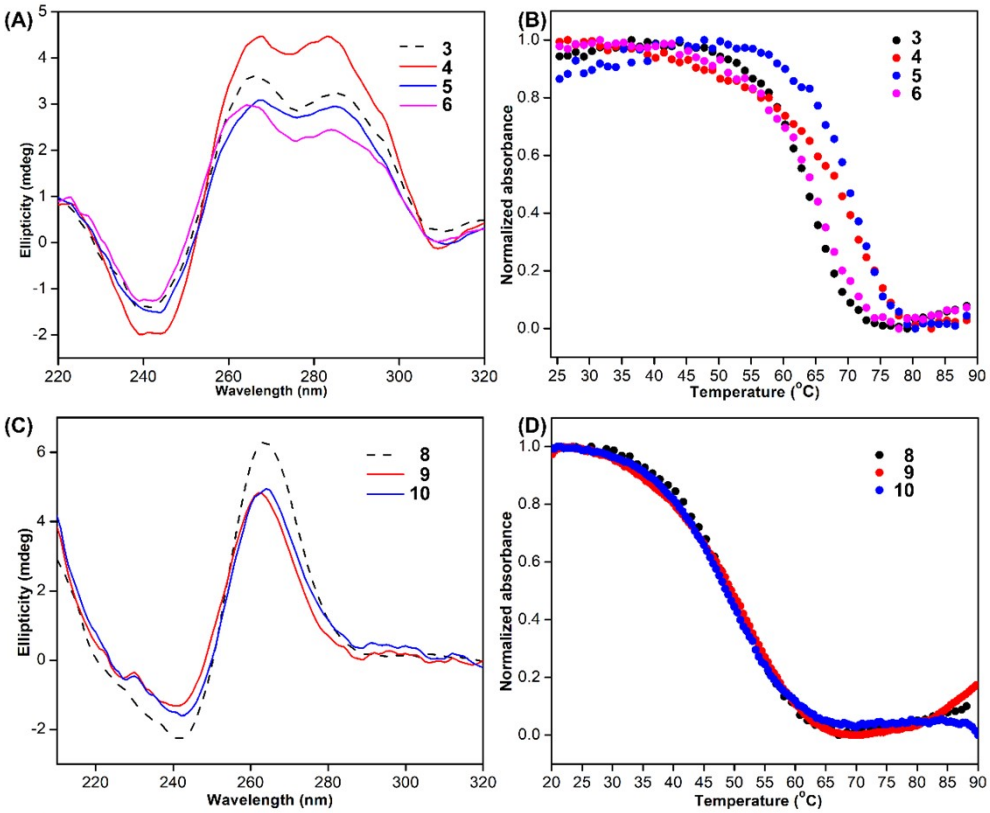

Fig. S3 (**A**) CD spectra of control LTR-III ON **3** (5 µM), modified LTR-III ONs **4**–**6** (5 µM). (**B**) UV-thermal melting profiles for the same at 295 nm (2 µM). (**C**) CD spectra of control LTR-IV ON **8** (8 µM), modified LTR-IV ONs **9** and **10** (8 µM). (**D**) UV-thermal melting profiles for the same at 295 nm (5 µM). See Table S2 for T_m values.

Table S2. T_m values of modified and control unmodified ONs.[a]

	LTR-III ONs	T_m (°C)	LTR-IV ONs	T_m (°C)	LTR-III + IV ONs	T_m (°C)
control unmodified ONs	**3**	65.0 ± 0.7	**8**	51.6 ± 0.3	**12**	55.6 ± 0.2
modified ONs	**4**	69.4 ± 1.6	**9**	52.2 ± 0.7	**13**	60.6 ± 0.3
	5	69.0 ± 1.7	**10**	51.6 ± 1.2	**14**	55.6 ± 0.4
	6	64.8 ± 0.7			**15**	56.5 ± 0.3
					16	55.2 ± 0.4

[a] Standard deviation reported from triplicate measurements.

7. Steady-state fluorescence of modified LTR ONs: LTR GQ structures of ONs **4** (0.5 μM), **9** (1 μM) and **10** (1 μM) were formed by heating the samples at 95 °C for 5 min in 20 mM potassium phosphate buffer (pH 7) containing 70 mM KCl. The corresponding duplexes **4•7**, **9•11** and **10•11** were prepared by heating a 1:1.1 mixture of LTR ONs **4**, **9** and **10** with complementary ONs **7** and **11** at 95 °C for 5 min in the same ionic conditions as mentioned above. All the samples were cooled slowly to RT. Experiments were done in triplicate in a micro-fluorescence cuvette (Hellma, path length 1.0 cm) on a Fluoromax-4 spectrofluorometer (Horiba Scientific) at 25 °C.

8. NMR of LTR ONs: LTR GQ structures of ONs **3**–**6** (45 μM), **8** (75 μM), **9** (10 μM or 75 μM), **10** (75 μM), **13**–**16** (45 μM) were formed by heating the samples at 95 °C for 5 min in 20 mM potassium phosphate buffer (pH 7) containing 70 mM KCl in 20% D_2O. The corresponding duplexes **4•7** and **9•11** were prepared by heating a 1:1.1 mixture of LTR ONs **4** and **9** with complementary ONs **7** and **11** respectively at 95 °C for 5 min in the same ionic conditions as mentioned above. ^{19}F and ^{1}H NMR spectra were acquired at a frequency of 564.9 MHz and 600 MHz, respectively, on a Bruker AVANCE III HD ASCEND 600 MHz spectrometer equipped with CryoProbe (CP2.1 QCl 600S3 H/F-C/N-D-05 Z XT). All ^{19}F NMR spectrum were calibrated relative to an external standard, trifluorotoluene (TFT = −63.72 ppm). Spectral parameters for ^{19}F NMR: excitation pulse: 12 μs; spectral width: 90.32 ppm; transmitter frequency offset: -145 ppm; acquisition time: 0.33 s; relaxation delay: 1.0 s; number of scans: 5000–6000. Using these parameters, spectra were obtained in 2–2.5 h. Each spectrum was processed with an exponential window function using lb = 20 Hz. ^{1}H NMR spectra were obtained with water suppression using excitation sculpting with gradients. Number of scans was 1200.

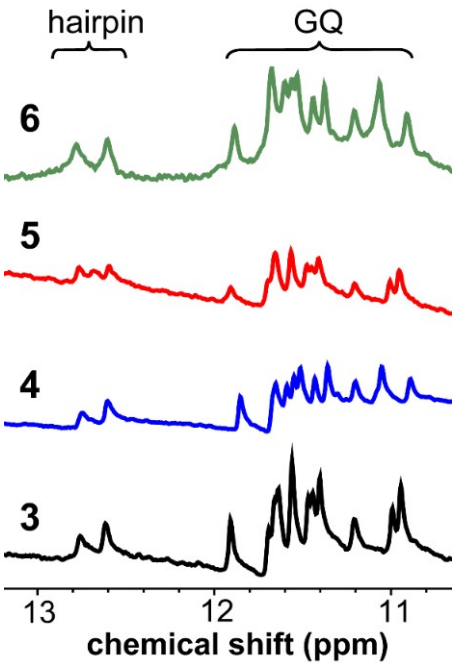

Fig. S4 Partial ^{1}H NMR spectra (45 µM) of control ON **3** and modified ONs **4**–**6**. For details see Section 8.

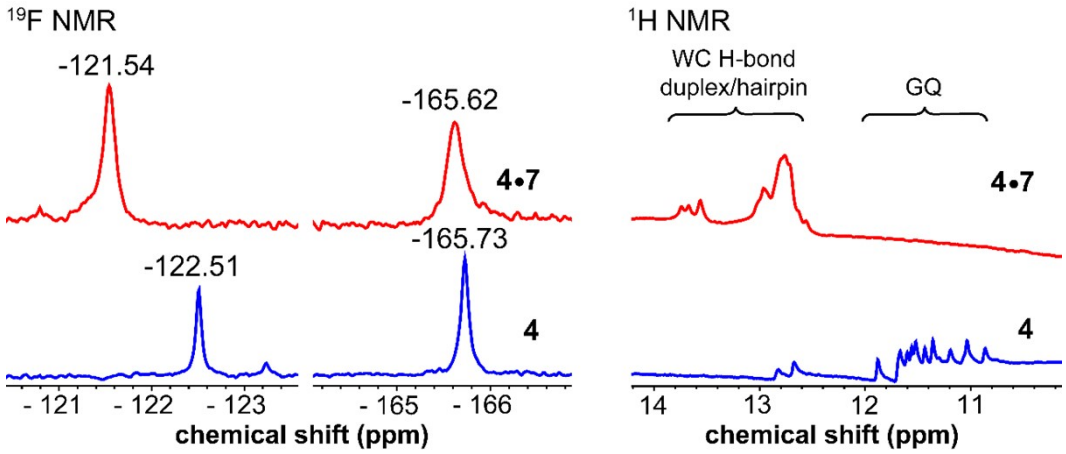

Fig. S5 ^{19}F and ^{1}H NMR spectra (45 µM) of ON **4** and its duplex **4•7**. For details see Section 8.

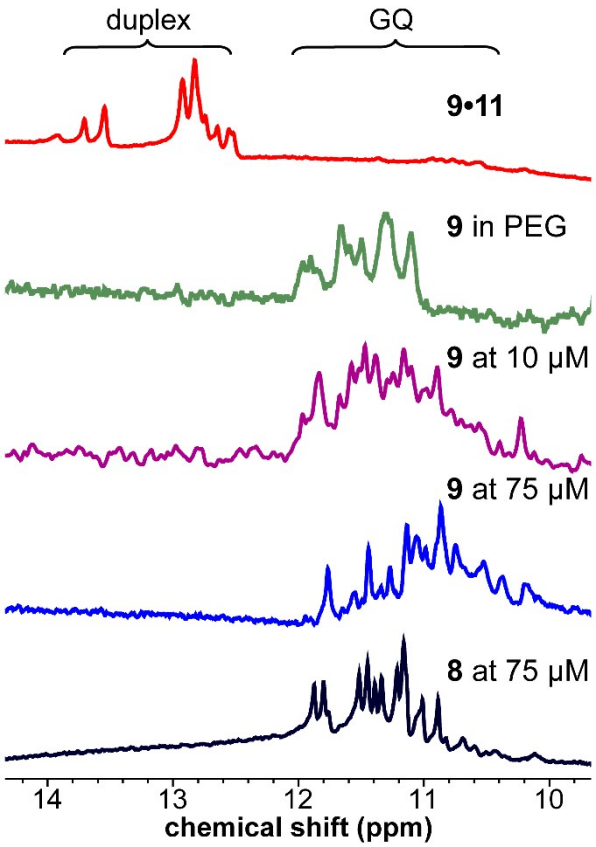

Fig. S6 Partial ^{1}H NMR spectra of control ON **8** (75 µM) and FBFdU-modified ON **9** under different conditions. For details see Section 8.

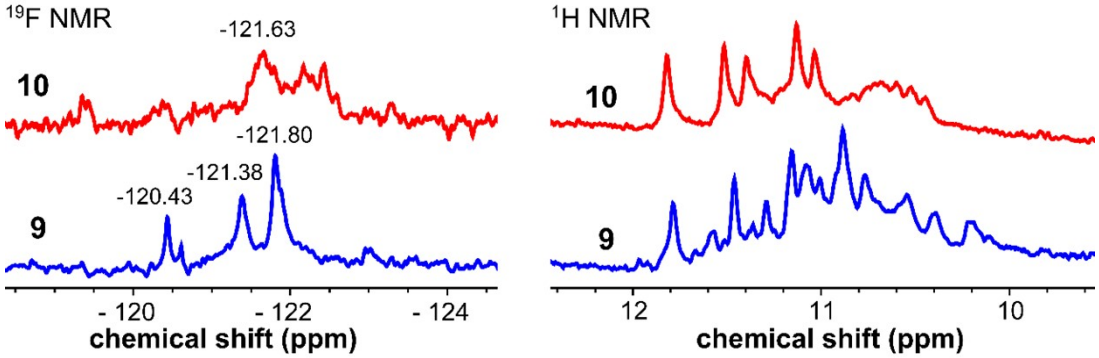

Fig. S7 ^{19}F and ^{1}H NMR spectra of ONs **9** and **10.** For details see Section 8.

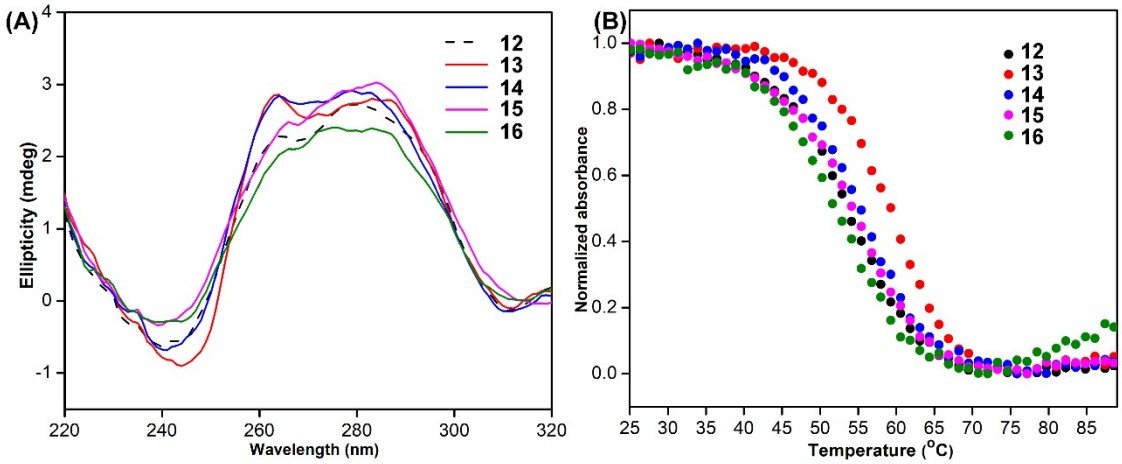

Fig. S8 (**A**) CD spectra of control LTR-(III+IV) ON **12** (5 µM), modified LTR-(III+IV) ONs **13**–**16** (5 µM). (**B**) UV-thermal melting profiles for the same at 295 nm (2 µM). See Section 5 and 6 for experimental details

9. Preparation of ON 16 for ^{19}F NMR analysis in intraoocyte buffer, lysate and egg extract.

An adult female *Xenopus laevis* was anesthetized and its oocytes were surgically removed following the protocol approved by the Institutional Animal Ethics Committee (IAEC), Indian Institute of Science Education and Research (IISER) Bhopal. All experiments that employed *Xenopus laevis* oocytes were performed in accordance with a protocol approved by the Institutional Animal Ethics Committee (IAEC) (proposal application number 2023-IISERB-01-IEAC), IISER Bhopal following the guidelines prescribed by the Committee for the Purpose of Control and Supervision of Experiments on Animals (CPCSEA), Government of India.

In IO buffer: ^{1}H NMR and ^{19}F NMR spectra of ON **16** (100 µM) annealed in IO buffer containing 20% D_2O were recorded at a frequency of 564.9 MHz and 600 MHz (25 °C), respectively. Spectral parameters are the same as mentioned in Section 8. ^{19}F NMR (number of scans = 6000) and ^{1}H NMR (number of scans = 1500). ^{19}F NMR spectra were processed with an exponential window function using lb = 20 Hz.

In egg lysate: Near 280 healthy *Xenopus laevis* oocytes (stage V/VI) were selected and kept in an ice-cold petri-dish containing 15 mL of Ori-Ca^{2+} buffer (5 mM HEPES (pH 7.5), 110 mM NaCl, 5 mM KCl, 2 mM $CaCl_2$, and 1 mM $MgCl_2$) for 15 min. Oocytes were washed with ice-cold Ori-Ca^{2+} buffer (15 mL). The buffer was removed and oocytes were resuspended in IO buffer (15 mL, 15 min). This step was repeated two more times. Oocytes were transferred to a centrifuge tube and allowed to settle down. The excess buffer was removed carefully without disturbing the settled oocytes. Oocytes were again washed with 200 µL of IO buffer containing 20% D_2O (repeated two times). Eggs were finally resuspended in 200 µL of IO buffer containing 20% D_2O and mechanically crushed. The suspension was centrifuged at 20000g (at 4 °C) for 10 min. The interphase layer was transferred to another centrifuge tube and heat denatured at 95 °C for 10 min. The sample was centrifuged at 20000g (4 °C, 10 min) and the clear lysate (300 µL) was transferred to another centrifuge tube and stored at 4 °C. ON **16** (1 mM, 30 µL) annealed in IO buffer containing 20% D_2O was added to the clear lysate (270 µL) and mixed well. The final sample volume was 300 µL containing 100 µM of the ON. The sample was incubated for 30 min at 4 °C

and then brought to 25 °C before recording the NMR using following parameters. ^{19}F NMR (number of scans = 6000) and ^{1}H NMR (number of scans = 1500) spectra were acquired at a frequency of 564.9 MHz and 600 MHz (25 °C), respectively. Spectral parameters are the same as mentioned in Section 8. ^{19}F NMR spectra were processed with an exponential window function using lb = 20 Hz. After the analysis, the sample was stored at -20 °C and analyzed by RP-HPLC to study the integrity of the ON in cell lysate during the NMR acquisition time. Sample was filtered using a centrifuge spin filter. The centrifuge tube was washed with 50 µL of water. The combined solution was analyzed by RP-HPLC and the fraction corresponding to ON **16** was further analyzed by ESI-MS (Figure S11 and S12).

In egg extract: 850–900 healthy oocytes were transferred into a petri-dish containing cold Ori-Ca^{2+} buffer (15 mL) and kept for 15–20 min. The eggs were then shifted to another petri-dish containing ice-cold IO buffer and incubated for 15 min. The oocytes were washed with ice-cold IO buffer (2 x 15 mL) and transferred to a centrifuge tube. Buffer above the oocytes was removed carefully after they settled down. Oocytes were washed with IO buffer (400 µL) containing 20% D_2O (repeated two times). After the centrifugation of the oocytes at 400g for 1 min at 4 °C, the supernatant buffer was removed carefully. The oocytes were again supplemented with intraoocyte buffer (100 µL) containing 20% D_2O and centrifuged at 12000g for 5 min at 4 °C. The eggs were crushed mechanically and the suspension was centrifuged at 12000g for 30 min at 4 °C to obtain the interphase layer. This crude interphase layer was directly used for the NMR analysis. 2 mM of the preannealed ON **16** (15 µL) in IO buffer containing 20% D_2O was added to the above crude egg extract (285 µL) and incubated for 30 min at 4 °C. The final sample volume was 300 µL containing 100 µM of the ON. The ^{19}F (number of scans = 6000) and ^{1}H NMR (number of scans = 4000) spectra were recorded at a frequency of 564.9 MHz and 600 MHz at 25 °C, respectively. Spectral parameters are the same as mentioned above. The ^{19}F NMR spectrum was processed with an exponential window function using lb = 20 Hz.

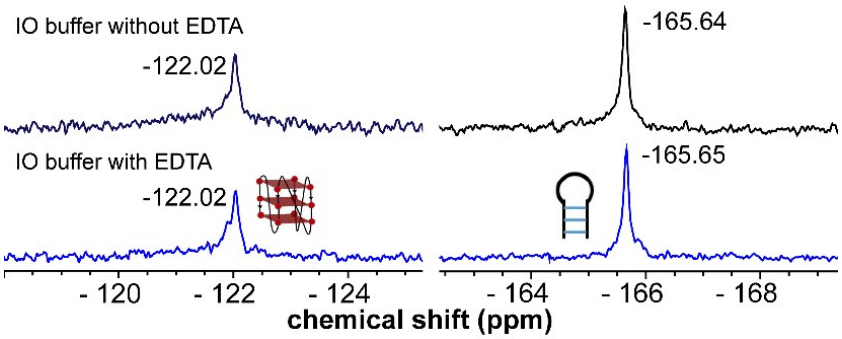

Fig. S9 ^{19}F NMR of ON **16** (100 µM) in IO buffer without EDTA (black line) and IO buffer with EDTA (blue line). We obtained peaks with almost the same chemical shifts in the absence and presence of EDTA. In NMR experiments with frog egg lysate and extract we used a small amount of EDTA as it is usually used in intracellular and lysis buffers to reduce the degradation of DNA from nucleases.[S4,S5] It is to be noted that the presence or absence of EDTA did not affect the NMR analysis.

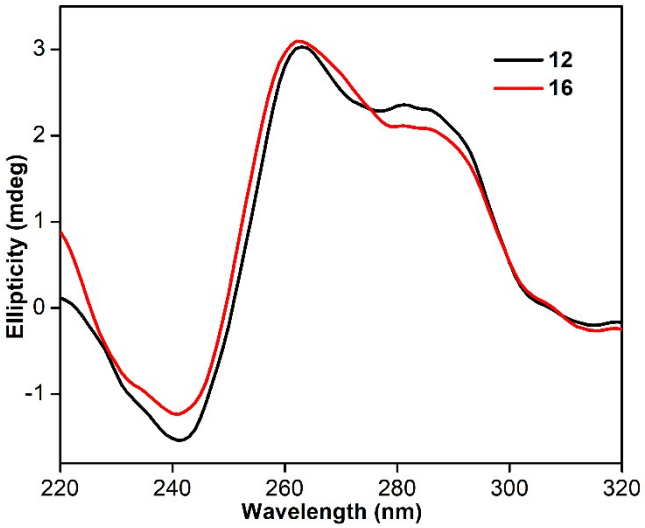

Fig. S10 CD spectra of ONs **12** and **16** each at 5 µM in intraoocyte (IO) buffer. See Section 5 for details.

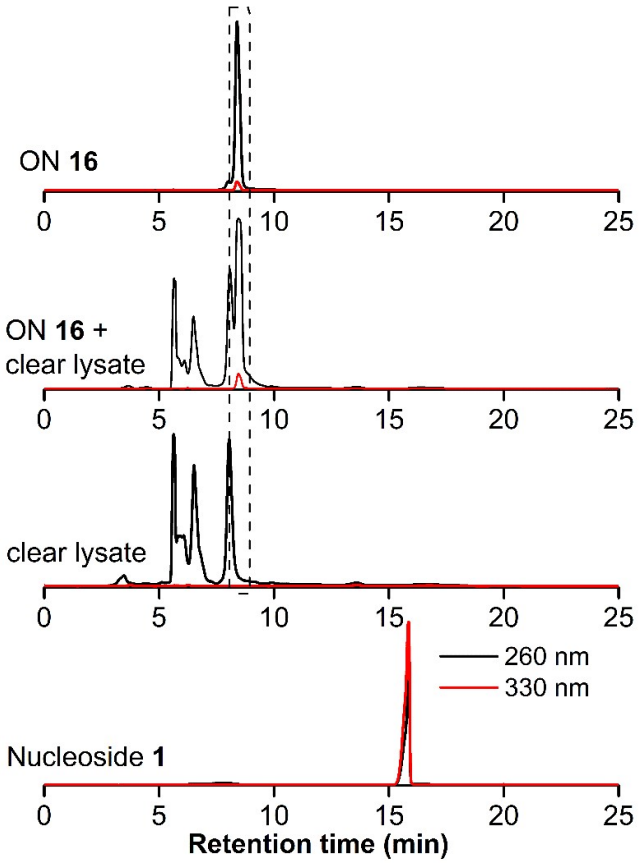

Fig. S11 Comparison of RP-HPLC chromatogram of ON **16**, **16** in lysate after the NMR experiments, lysate (control) and nucleoside FBFdU **1** at 260 nm and 330 nm. ON **16** is stable in the lysate and no detectable degradation of ON **16** was observed (see the peak within the dashed line). Peaks between 5–8 min are from metabolites of the clear lysate.

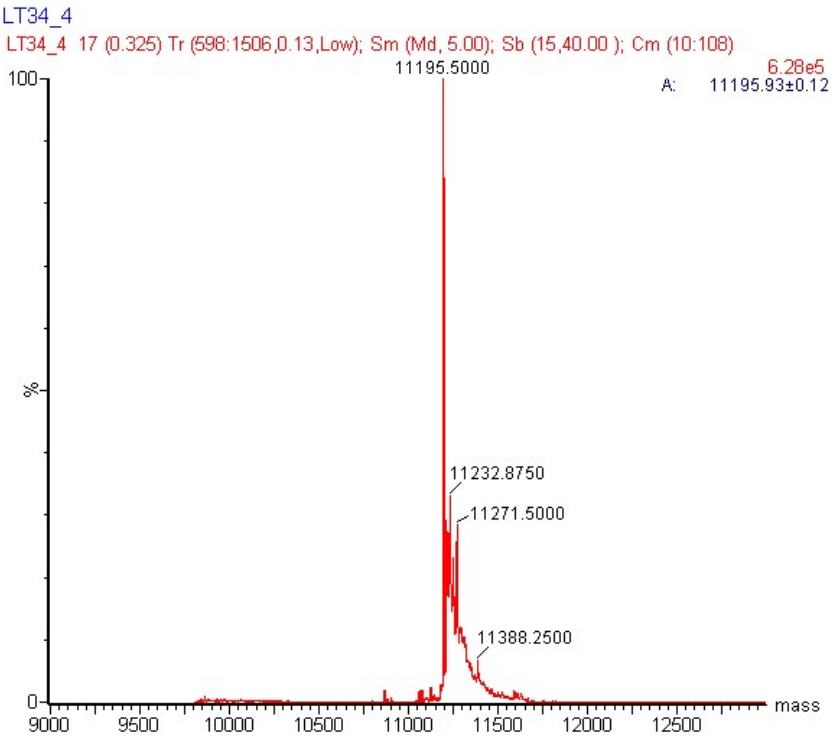

Fig. S12 ESI-MS spectra of modified ON **16** extracted from lysate sample after NMR analysis (calculated mass = 11194.75, observed mass =11195.50).

Table S3. Absorbance and emission wavelengths of nucleoside FBFdU (**1**) in different solvents. Data reported from J. Am. Chem. Soc. 2018, 140, 12622–12633.[S1]

solvent	λ_{max} (nm)	λ_{em} (nm)	Φ
water	322	437	0.11
methanol	322	418	0.04
dioxane	324	400	0.03
ethylene glycol	325	420	0.20
glycerol	326	424	0.52

Table S4. ^{19}F NMR chemical shift (ppm) of FBFdU (**1**) and FdU (**2**) in different solvents.[S1, S2]
Although ^{19}F label exhibits distinct chemical shifts in different solvents, the trend based on polarity and viscosity order is complex.

solvent	FBFdU	FdU
water	-121.78	-166.49
methanol	-123.70	-169.39
dioxane	-123.01	-169.06
ethylene glycol	-122.35	-168.05

10. Computational analysis: Molecular dynamics (MD) simulations were carried out using the templates HIV LTR-III (PDB ID: 6H1K)[S6] LTR-IV (PDB ID:2N4Y)[S7]. Force field parameters were generated for FdU and FBFdU to prepare the ON structures with the probes. Both structures were prepared using GaussView 6.0 with phosphate capping at both 3' and 5' ends. FBFdU has a rotatable bond between the fluorophore and the base. A dihedral scan was performed for FBFdU with 36 rotations of 10 degrees each in Gaussian 16 version B.01[S8] at theory

level HF/6-31G* to find the most stable conformer. The stable conformer showing the lowest potential energy was then optimized in Gaussian 16 at the same theory level. FdU was also optimized using a similar strategy. ESP charges were calculated using Gaussian 16, and RESP fitting was done in the antechamber[S9] module of AmberTools 19. The parmchk2 program generated an initial set of force field parameters. However, some were missing parameters, and others had high penalty scores. The capping was then removed, and after fixing the overall charges, the GAFF[S10] library was used to fill in the missing parameters. Finally, prepin files were generated for complex preparation.

These modifications were incorporated into their respective templates in tleap. Central K^+ of the GQ core was also added using manual coordinate calculations. The complex was solvated with a rectangular water box using TIP3PBOX force field having an edge length of 10 Å. ~27 K^+ were added to neutralize the system. OL15[S11] was used to define the DNA. MD simulations were carried out using our previously reported protocol.[S10] Briefly, all the complexes were subjected to 10,000 steps of restrained minimization by the steepest descent method with a restraint of 2.0 kcal/mol. $Å^2$ followed by 100 ps of heating and 100 ps of density equilibration. Further, 800 ps of NPT equilibration and 500 ns of production run were carried out in GPU accelerated version of PMEMD[S13-S15] in AMBER 18.[S16] A total of ~2.5 µs (5*500 ns) simulations were carried out. The SHAKE algorithm was applied to subject the hydrogens to bond length constraints. All the MD analyses were carried out using the CPPTRAJ[S17] module of AmberTools 19. The hierarchical agglomerative algorithm was used for clustering the trajectories. The cut-offs for stacking were a COM distance of 5 Å and a vector angle of 45 degrees. The trajectories were visualized using VMD,[S16] and images were rendered using PyMOL(Schrodinger LLC.)

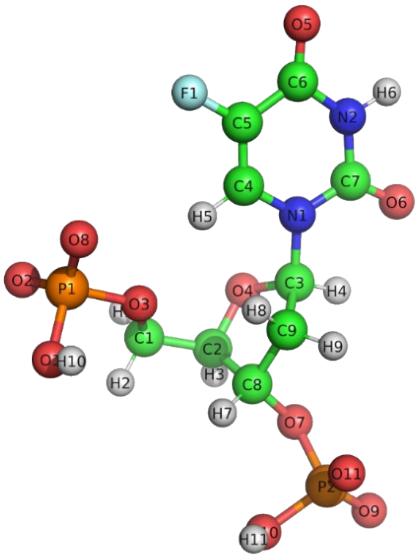


```
     0    0              2
  This is a remark line
molecule.res
  FDU             INT         0
  CORRECT         OMIT        DU       BEG
        0.0000
           1   DUMM        DU        M        0        -1        -2         0         0         0         0
           2   DUMM        DU        M        1         0        -1     1.449         0         0         0
           3   DUMM        DU        M        2         1         0     1.523    111.21         0         0
```

4	P1	P	M	3	2	1	1.54	111.208	-180	1.294462
5	O2	O2	E	4	3	2	1.469	81.307	-120.503	-0.909793
6	O8	O2	E	4	3	2	1.472	46.311	76.917	-0.909793
7	O3	OS	M	4	3	2	1.646	110.787	-13.801	-0.640503
8	C1	CT	M	7	4	3	1.398	120.517	-120.842	0.144315
9	H1	H1	E	8	7	4	1.083	110.027	63.971	0.038448
10	H2	H1	E	8	7	4	1.086	110.759	-55.331	0.038448
11	C2	CT	M	8	7	4	1.516	109.506	-175.355	0.10031
12	H3	H1	E	11	8	7	1.083	108.884	179.331	0.068969
13	O4	OS	S	11	8	7	1.426	109.53	-62.744	-0.471067
14	C3	CT	3	13	11	8	1.392	111.377	121.413	0.280157
15	H4	H2	E	14	13	11	1.075	110.454	103.214	0.089924
16	N1	N*	S	14	13	11	1.474	108.136	-141.827	-0.385478
17	C4	CM	B	16	14	13	1.383	119.469	52.773	0.047923
18	H5	H4	E	17	16	14	1.075	116.654	3.002	0.233236
19	C5	CM	B	17	16	14	1.328	121.991	-176.865	-0.094409
20	C6	C	B	19	17	16	1.45	121.491	0.422	0.642038
21	O5	O	E	20	19	17	1.2	127.066	179.948	-0.707254
22	N2	NA	B	20	19	17	1.38	111.743	0.057	-0.646274
23	H6	H	E	22	20	19	0.997	116.47	179.661	0.304756
24	C7	C	S	22	20	19	1.379	128.863	0.555	0.73023
25	O6	O	E	24	22	20	1.2	119.961	178.871	-0.727943
26	F1	F	E	19	17	16	1.327	122.327	179.93	-0.148638
27	C9	CT	B	14	13	11	1.524	106.529	-18.129	-0.132195
28	H8	HC	E	27	14	13	1.082	110.583	-84.598	0.063958
29	H9	HC	E	27	14	13	1.08	113.265	151.624	0.063958
30	C8	CT	M	11	8	7	1.537	115.49	56.62	0.179574
31	H7	H1	E	30	11	8	1.081	111.369	22.658	0.078991
32	O7	OS	M	30	11	8	1.402	107.933	144.829	-0.626347
LOOP										
C7	N1									
C8	C9									
IMPROPER										
C7	C4	N1	C3							
C5	H5	C4	N1							
C6	C4	C5	F1							
C5	N2	C6	O5							
C6	C7	N2	H6							
N1	N2	C7	O6							
DONE										
STOP										

Fig. S13 Cartesian coordinates and RESP charges calculated for the FdU adduct generated using Gaussian 16. Carbons atoms are represented by green, nitrogen atoms by blue, oxygen atoms by red, fluorine by cyan and hydrogen atoms by white respectively.

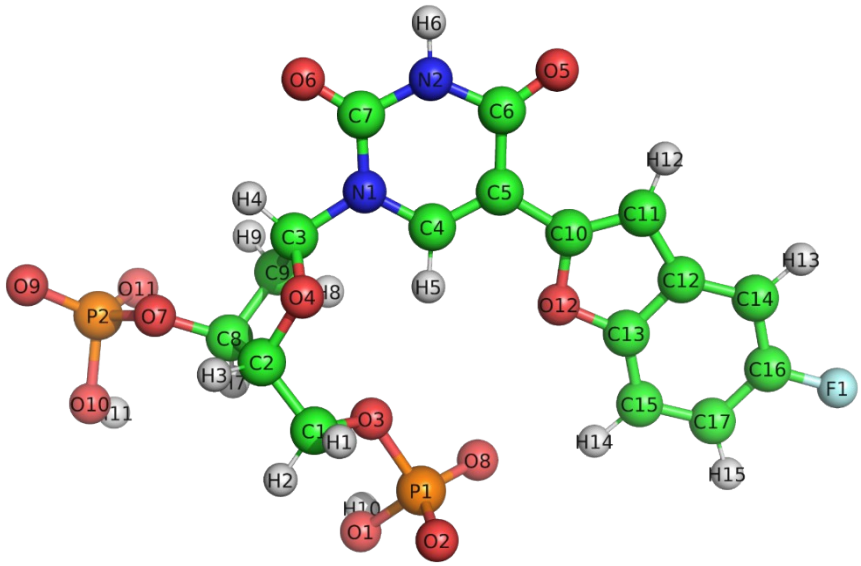

0 0 2
This is a remark line
molecule.res
FBFDU INT 0
CORRECT OMIT DU BEG
0.0000

1	DUMM	DU	M	0	-1	-2	0	0	0	0
2	DUMM	DU	M	1	0	-1	1.449	0	0	0
3	DUMM	DU	M	2	1	0	1.523	111.21	0	0
4	P1	P	M	3	2	1	1.54	111.208	-180	1.329951
5	O2	O2	E	4	3	2	1.469	102.542	-69.037	-0.907294
6	O8	O2	E	4	3	2	1.477	133.025	105.246	-0.907294
7	O3	OS	M	4	3	2	1.644	57.297	-173.44	-0.629415
8	C1	CT	M	7	4	3	1.402	118.04	54.604	0.143944
9	H1	H1	E	8	7	4	1.084	109.87	71.765	0.042331
10	H2	H1	E	8	7	4	1.086	110.559	-47.174	0.042331
11	C2	CT	M	8	7	4	1.514	110.845	-167.033	0.101983
12	H3	H1	E	11	8	7	1.083	108.375	176.116	0.071046
13	O4	OS	S	11	8	7	1.429	109.832	-66.203	-0.463418
14	C3	CT	3	13	11	8	1.391	110.667	128.117	0.279273
15	H4	H2	E	14	13	11	1.077	111.028	96.849	0.094203
16	N1	N*	S	14	13	11	1.475	107.506	-147.989	-0.379024
17	C4	CM	B	16	14	13	1.364	119.403	52.105	0.123751
18	H5	H4	E	17	16	14	1.075	114.89	2.014	0.233422
19	C5	CM	B	17	16	14	1.35	123.996	-177.596	-0.298709
20	C6	C	B	19	17	16	1.455	118.481	1.281	0.680537
21	O5	O	E	20	19	17	1.202	127.194	179.279	-0.708119
22	N2	NA	B	20	19	17	1.381	113.242	-0.56	-0.638327
23	H6	H	E	22	20	19	0.997	116.23	179.821	0.311693
24	C7	C	S	22	20	19	1.373	128.831	0.532	0.743339
25	O6	O	E	24	22	20	1.197	120.755	179.188	-0.707045
26	C10	C*	S	19	17	16	1.461	121.17	-178.289	0.120509
27	C11	C*	B	26	19	17	1.347	133.367	-175.809	-0.216033
28	C12	CB	S	27	26	19	1.446	105.519	-179.349	-0.092125
29	C13	CB	B	28	27	26	1.389	105.35	0.092	0.052891
30	C15	CA	B	29	28	27	1.38	124.347	179.52	-0.068718
31	C17	CA	B	30	29	28	1.38	116.104	0.291	-0.19327
32	C16	CA	B	31	30	29	1.39	119.966	-0.033	0.074936
33	C14	CA	S	32	31	30	1.372	123.833	-0.186	-0.165353

34	H13	HA	E	33	32	31	1.075	120.429	-179.75	0.122269
35	F1	F	E	32	31	30	1.346	117.813	-179.963	-0.18672
36	H15	HA	E	31	30	29	1.074	121.136	179.921	0.1269
37	H14	HA	E	30	29	28	1.078	119.977	-179.04	0.228791
38	O12	OS	E	29	28	27	1.35	109.737	-0.162	-0.17201
39	H12	HA	E	27	26	19	1.066	125.988	0.284	0.160246
40	C9	CT	B	14	13	11	1.522	105.968	-24.509	-0.132497
41	H8	HC	E	40	14	13	1.083	110.505	-79.957	0.065488
42	H9	HC	E	40	14	13	1.079	113.784	155.703	0.065488
43	C8	CT	M	11	8	7	1.538	115.921	53.869	0.183496
44	H7	H1	E	43	11	8	1.081	111.413	19.034	0.083087
45	O7	OS	M	43	11	8	1.401	107.861	141.357	-0.616531
LOOP										
C7	N1									
O12	C10									
C14	C12									
C8	C9									
IMPROPER										
C7	C4	N1	C3							
C5	H5	C4	N1							
C10	C6	C5	C4							
C5	N2	C6	O5							
C6	C7	N2	H6							
N1	N2	C7	O6							
C11	C5	C10	O12							
C10	C12	C11	H12							
C11	C14	C12	C13							
C15	C12	C13	O12							
C17	C13	C15	H14							
C15	C16	C17	H15							
C17	C14	C16	F1							
C16	C12	C14	H13							
DONE										
STOP										

Fig. S14 Cartesian coordinates and RESP charges calculated for the FBFdU adduct generated using Gaussian 16. Carbons atoms are represented by green, nitrogen atoms by blue, oxygen atoms by red, fluorine by cyan and hydrogen atoms by white respectively.

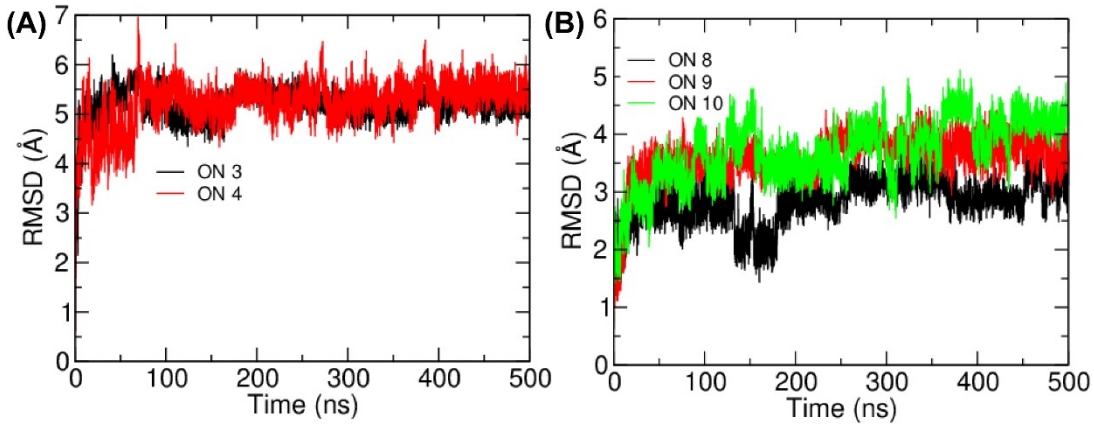

Fig. S15 RMSD plot of (**A**) LTR-III ON **3** and ON **4** (**B**) LTR-IV ON **8**, ON **9** and ON **10**. RMSD values were calculated from the 500 ns MD simulations.

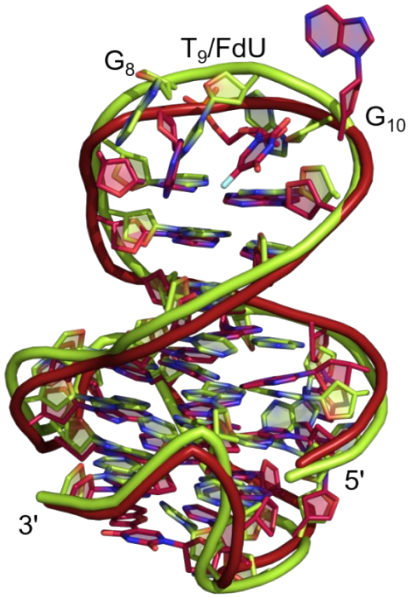

Fig. S16 Superimposed images of the major clusters of LTR-III native ON **3** and modified ON **4**. ON **3** and **4** are represented in green and maroon, respectively. The bases, which show maximum changes in the orientation are labeled in the Figure. The clusters have been obtained from the 500 ns MD simulation. The incorporation of FdU results in the partial stacking of FdU with G_8 and alters the orientation slightly from the native form while FBFdU remains the same. Model for ON **4** is available with the private link and access code (password): https://www.modelarchive.org/doi/10.5452/ma-okc7y
Code: QwwKvEyOwE

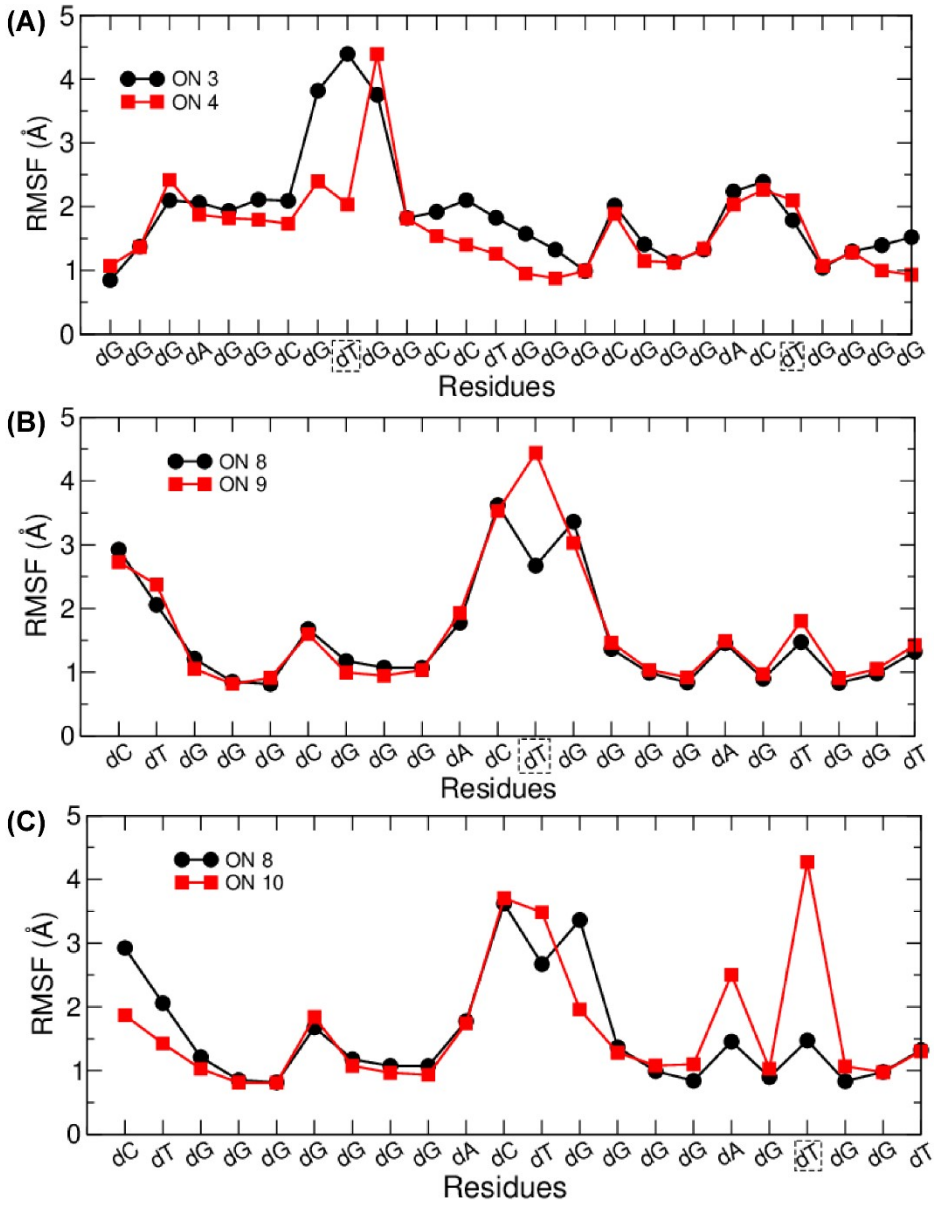

Fig. S17 RMSF plots of (**A**) LTR-III ON **3** and ON **4** with variation in the G_8 and FdU (**B**) LTR-IV ON **8** and ON **9** (**C**) LTR-IV ON **8** and ON **10** with variation in the probe. The nucleotides are represented from 5′ to 3′. The position of the probe has been indicated by a dashed box around the nucleotide RMSF values were calculated from the 500 ns MD simulations.

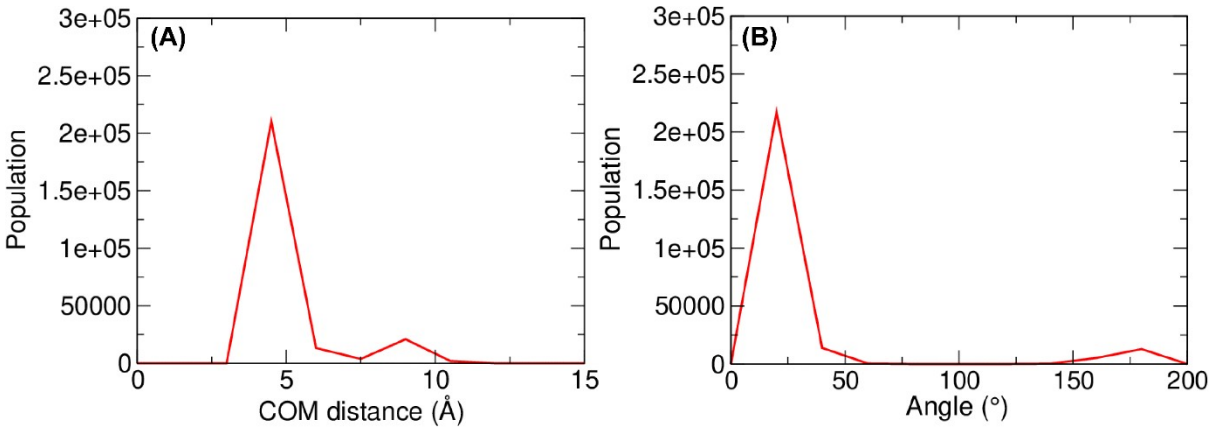

Fig. S18 Population distribution of the (**A**) centre of mass distance (COM) distance between G_{28} and FBFdU in ON **4**, (**B**) angle between the normal to G_{28} and FBFdU. The values were calculated from the 500 ns MD simulations.

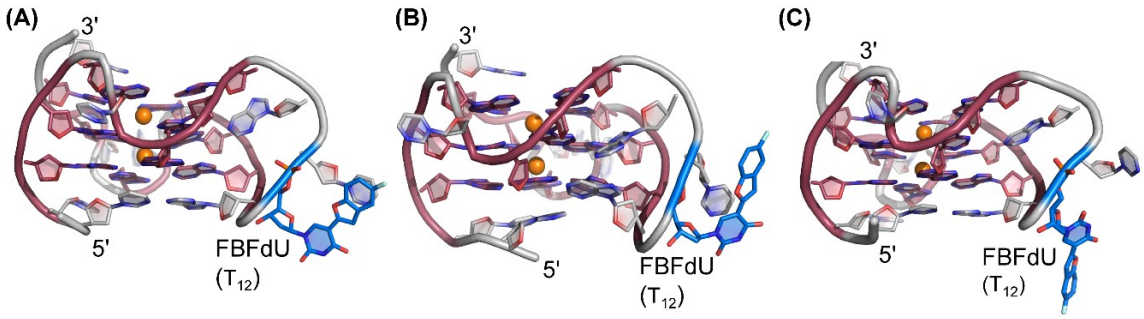

Fig. S19 Representative images of three major clusters of LTR-IV ON **9**. (**A**) Cluster 1, (**B**) cluster 2 and (**C**) cluster 3. GQ bases are represented in maroon and FBFdU in blue. K^+ ions are represented as orange spheres. Clusters have been obtained from the 500 ns MD simulation.
Model for ON **9** is available with the private link and access code (password): https://www.modelarchive.org/doi/10.5452/ma-6pmie Code: DG4iRTmwIz

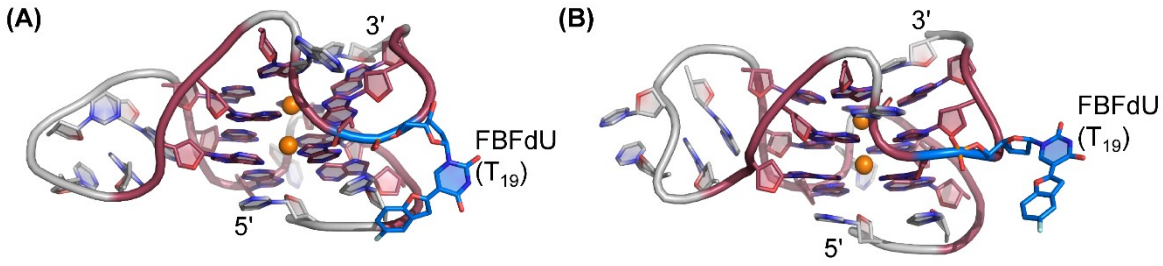

Fig. S20 Representative images of two major clusters of LTR-IV ON **10**. (**A**) Cluster 1 and (**B**) cluster 2. GQ bases are represented in maroon and FBFdU in blue. K^+ ions are represented as orange spheres. Clusters have been obtained from the 500 ns MD simulation. Model for ON **10** is available with the private link and access code (password): https://www.modelarchive.org/doi/10.5452/ma-otuxm
Code: INRqkxQXSJ

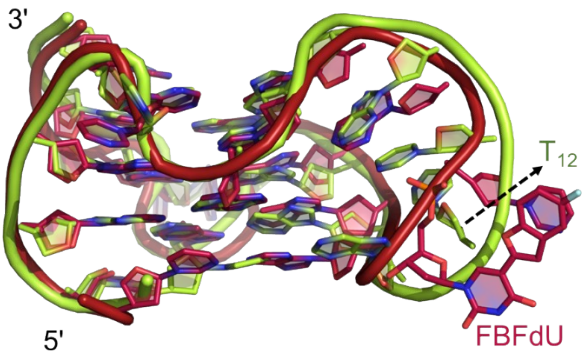

Fig. S21 Superimposed images of the major clusters of LTR-IV native ON **8** and modified ON **9**. ON **8** and **9** are represented in green and maroon, respectively. The bases, which show maximum changes in the orientation are labeled in the Figure. The clusters have been obtained from the 500 ns MD simulation.

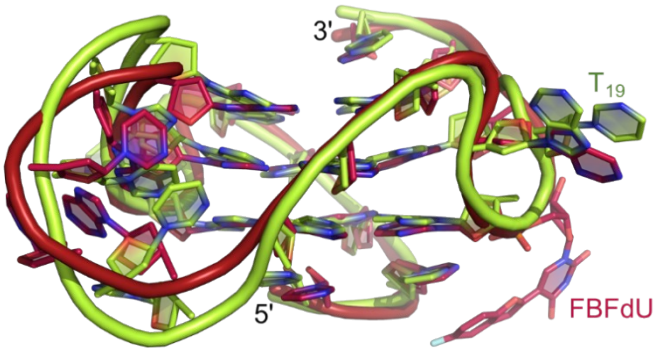

Fig. S22 Superimposed images of the major clusters of LTR-IV native ON **8** and modified ON **10**. ON **8** and **10** are represented in green and maroon, respectively. The bases, which show maximum changes in the orientation are labeled in the Figure. The clusters have been obtained from the 500 ns MD simulation.

11. Ligand binding studies of modified LTR ONs

Fluorescence: LTR GQ structures (0.5 μM) of ONs **4**, **9** and **16** were formed by heating the samples at 95 °C for 5 min in 20 mM potassium phosphate buffer (pH 7) containing 70 mM KCl. The samples were incubated with increasing concentrations of the ligands (TMPyP4 and BRACO19) at 25 °C for 1 h. Samples were excited at 330 nm with an excitation and emission wavelength slit widths of 7 nm and 9 nm, respectively. For DOX titration, increasing concentrations of annealed GQ formed by ON **12** in the same ionic conditions as mentioned above was incubated with DOX (2 μM) at 25 °C for 1 h. The final volume of each sample solution was kept at 200 μL. Samples were excited at 480 nm, with an excitation and emission slit widths of 7 nm and 9 nm respectively. Fluorescence experiments were performed in triplicate in a micro-fluorescence cuvette at 25 °C. For titration with TMPyP4 and BRACO19, an appropriate blank containing ligand in a buffer was subtracted from each reading for the corresponding ligand concentration. Normalized fluorescence intensity (F_N) against ligand concentration was plotted and fitted to a Hill equation (see below) to determine the apparent K_d values. Fitted graphs were prepared using OriginPro 8.5 software.[S19]

$$F_N = \frac{F_i - F_s}{F_0 - F_s}$$

F_i is the fluorescence intensity at each titration point. F_0 and F_s are the fluorescence intensity in the absence of ligand (L) and at saturation, respectively. n is the Hill coefficient or degree of cooperativity associated with the binding.

$$F_N = F_0 + (F_s - F_0)\left(\frac{[L]^n}{[K_d]^n + [L]^n}\right)$$

^{19}F NMR: LTR GQ structures of ONs **4** (45 μM), **9** (75 μM), **16** (45 μM) were formed by heating the samples at 95 °C for 5 min in 20 mM potassium phosphate buffer (pH 7) containing 70 mM KCl in 20% D_2O. The samples were allowed to cool at RT and then they were transferred to a Shigemi tube (5 mm advance NMR micro-tube) for NMR analysis. ^{19}F NMR spectra were recorded at a frequency 564.9 MHz on a Bruker AVANCE III HD ASCEND 600 MHz spectrometer equipped with Cryo-Probe (CP2.1 QCl 600S3 H/F-C/N-D-05 Z XT). After each experiment, increasing concentrations of ligands were added and incubated at RT for 1 h prior to the experiment. All ^{19}F NMR spectra were referenced relative to an external standard, trifluorotoluene (TFT = −63.72 ppm). Spectral parameters for ^{19}F NMR are same as mentioned in section 8. ^{19}F NMR spectra were obtained in 2–2.5 h with 5000–6000 scans. Spectra were processed with an exponential window function using lb = 20 Hz.

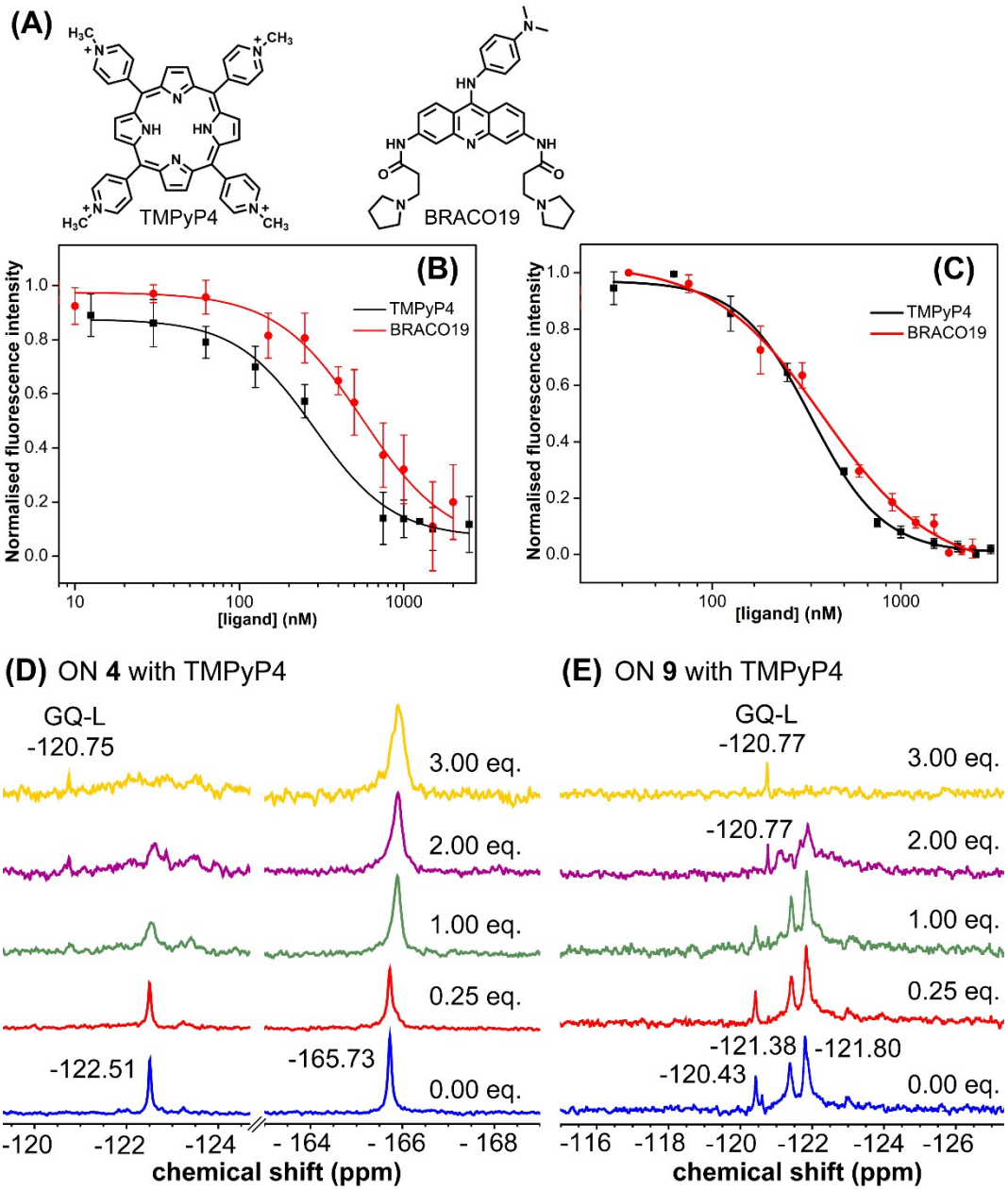

Fig. S23 (**A**) Chemical structures of GQ-binding ligands. Curve fits for the binding of TMPyP4 and BRACO19 to (**B**) LTR-III ON **4** and (**C**) LTR-IV ON **9**. Normalized fluorescence intensity at the emission maximum is plotted against ligand concentration. Values are denoted as mean ± s.d for 3 independent experiments. (**D** and **E**) ^{19}F NMR spectra of ONs **4** and **9** as a function of increasing TMPyP4 concentration. GQ-L represents peak corresponding to GQ-ligand complex.

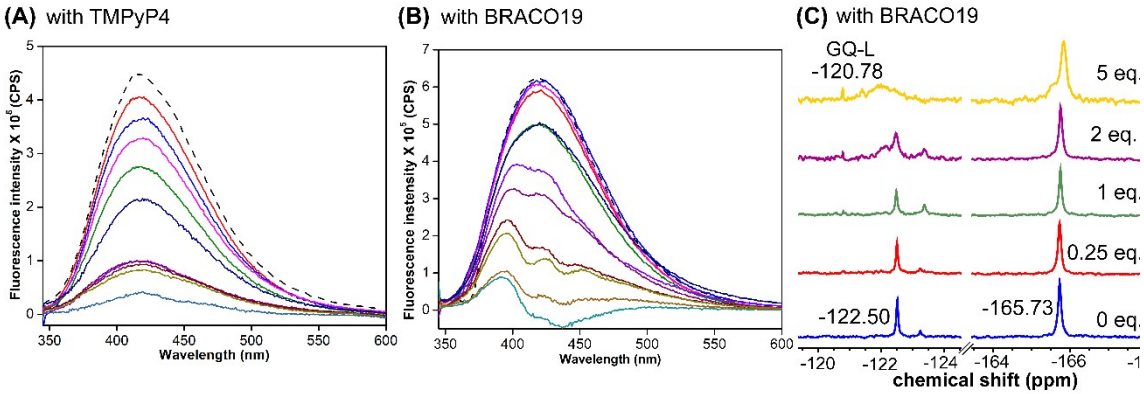

Fig. S24 Emission spectra for the titration of labeled LTR-III ON **4** (0.5 µM) with increasing concentration of (**A**) TMPyP4 (12.5 nM–2.5 µM) and (**B**) BRACO19 (10 nM–2.5 µM). Samples were excited at 330 nm with an excitation and emission slit widths of 7 nm and 9 nm, respectively. The dashed line represents the spectrum of ON **4** without any ligand. (**C**) ^{19}F NMR spectra of ON **4** (45 µM) with increasing BRACO19 concentration. GQ-L represents peak corresponding to GQ-ligand complex. See Section 11 for experimental details.

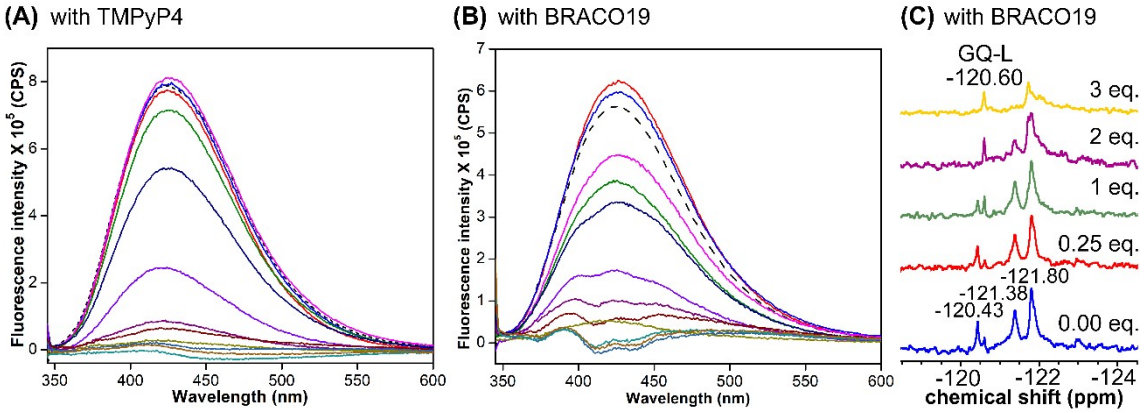

Fig. S25 Emission spectra for the titration of labeled LTR-IV ON **9** (0.5 µM) with increasing concentrations of (**A**) TMPyP4 (12.5 nM–2.5 µM) and (**B**) BRACO19 (36 nM–2.8 µM). Samples were excited at 330 nm with an excitation and emission slit widths of 7 nm and 9 nm, respectively. The dashed line represents the spectrum of ON **9** without any ligand. (**C**) ^{19}F NMR spectra of ON **9** (75 µM) with increasing BRACO19 concentration. GQ-L represents peak corresponding to GQ-ligand complex. See Section 11 for experimental details.

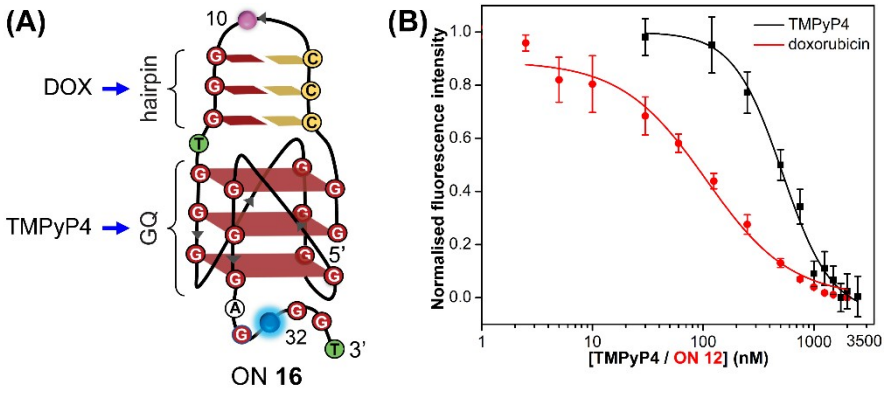

Fig. S26 FBFdU and FdU report structure-specific ligand binding to LTR GQ-hairpin structure. (**A**) Schematic representation of the doubly-labeled LTR ON **16** showing the preferred site of ligand (TMPyP4 to GQ and DOX to hairpin) interaction. (**B**) Curve fits for the binding of TMPyP4 and DOX to ON **16** (λ_{em}= 421 nm) and ON **12** (λ_{em}= 590 nm). Normalized fluorescence intensity at the emission maximum is plotted against ligand concentration. Values are denoted as mean ± s.d for 3 independent experiments. See Section 11 for experimental details.

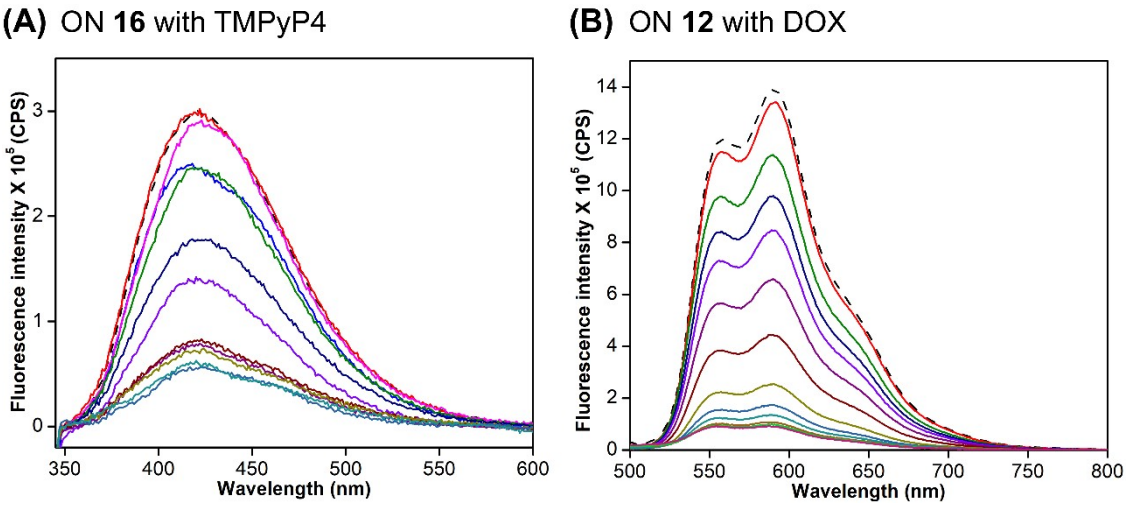

Fig. S27 (**A**) Emission spectra for the ligand titration of labeled LTR-(III+IV) ON **16** (0.5 µM) with increasing concentration of TMPyP4 (30 nM–2.5 µM). Samples were excited at 330 nm with an excitation and emission slit widths of 7 nm and 9 nm, respectively. The dashed line represents the spectrum of ON **16** without any ligand. (**B**) Emission spectra for the titration of DOX (2 µM) with increasing concentration of control ON **12** (2.5 nM–2.0 µM). Samples were excited at 480 nm with an excitation and emission slit widths of 7 nm and 9 nm, respectively. The dashed line represents the spectrum of DOX without any ON **12**.

12. *Taq* polymerase assay: 5′-FAM labeled primer **P1** (5 µM) and template DNA ONs **T1** and **T2** (5 µM) were annealed in 10 mM Tris-HCl (pH 7.8) containing 100 mM KCl at 95 °C for 5 minutes and slowly cooled to RT (Table S5). The primer-template duplexes were further diluted to 1 µM in 10 mM Tris-HCl buffer containing 100 mM KCl. Primer extension reactions were performed with primer-template duplex (100 nM), KCl (100 mM), 1× DNA polymerase buffer (10 mM Tris-HCl, pH 8.3, 50 mM KCl, 1.5 mM $MgCl_2$) at 37 °C. Reactions were initiated by adding dNTPs (500 µM) and 0.5 µL of *Taq* DNA polymerase (5 U/µL, New England Biolabs, Catlog. M0273S) in a total reaction volume of 20 µL. Reactions were stopped at different time intervals by adding 10 µL of denaturing

loading buffer (8.3 M urea in 10 mM Tris-HCl, 100 mM EDTA, 0.05% bromophenol blue, pH 8) further flash cooled on a dry-ice bath. The reaction mixture was then concentrated in a speedvac concentrator. The extension products were resolved by 15% denaturing PAGE containing 8.3 M urea and was electrophoresed at a constant power of 35 W for 2.5–3 h. The gel was scanned using an Amersham Typhon 600 (GE Healthcare) at the FAM wavelength and quantified with the help of the ImageJ software. Impact of ligands on the polymerase activity was studied by adding different concentrations of TMPyP4 and or DOX. The ligands were first added to the reaction mixture and incubated for 1 h at RT and then initiated by adding dNTPs and enzyme as above. The reaction products were analyzed as described above.

Table S5. Sequence of templates and primer used in *Taq* DNA polymerase stop assay.

ON	5′----------3′
P1	FAM-GGCAAAAAGCAGCTGCTTATATGCAG
T1	TTTTTGGGAGGCGTGGCCTGGGCGGGACTGGGGAGTGGTTTTTCTGCATATAAGCAGCTGCTTTTTGCC
T2[a]	TTTTTGGGAGGCGTGGCCTG**T**GCG**T**GACTGGGGAGTGGTTTTTCTGCATATAAGCAGCTGCTTTTTGCC

[a]**T** represents G-T mutation. This mutation does not support GQ formation.[S20]

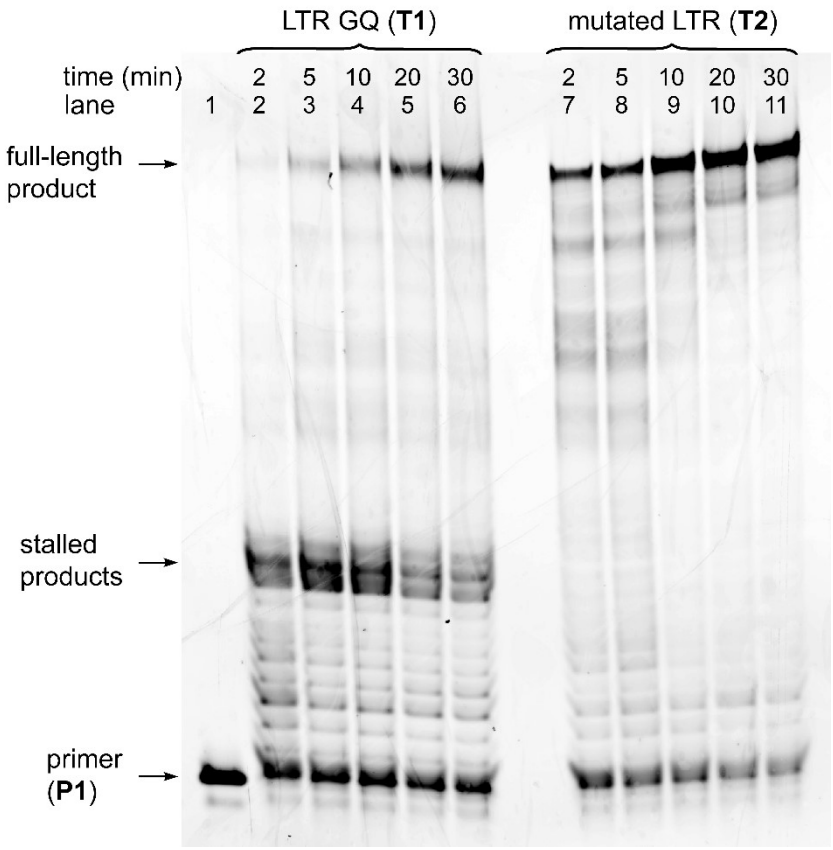

Fig. S28 Gel image of primer extension reactions using native LTR G-rich ON template **T1** and mutated LTR template **T2**. See Section 12 for details.

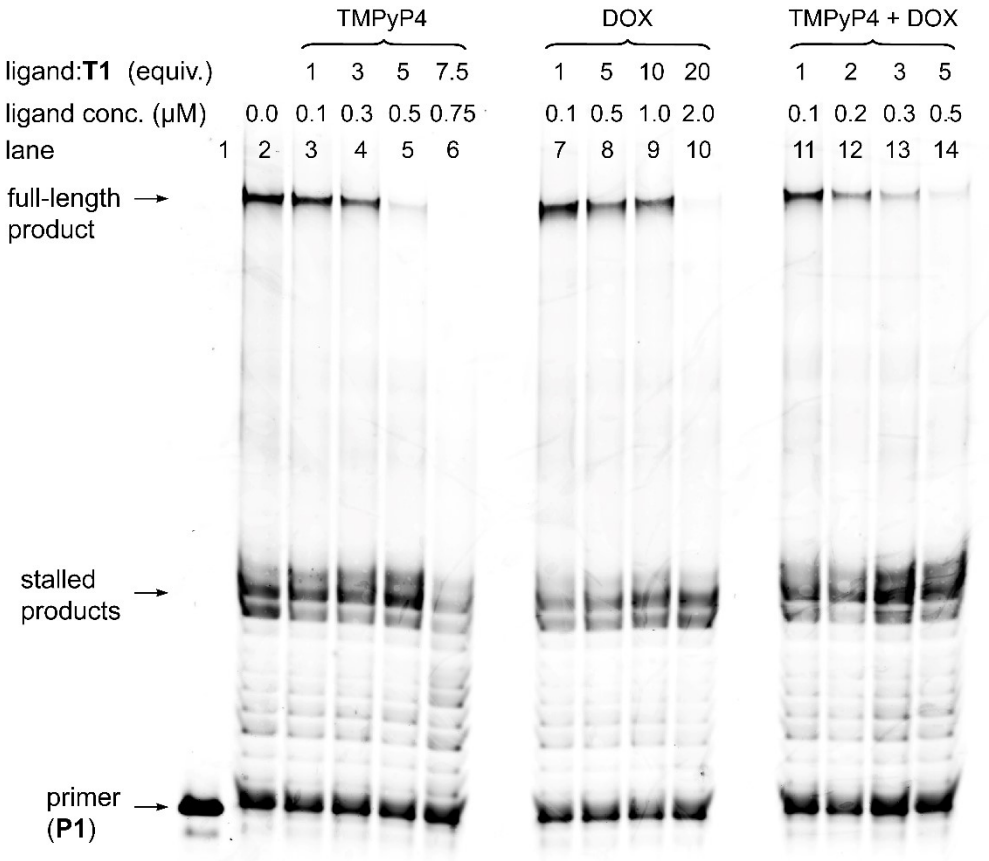

Fig. S29 Gel image of primer extension reactions using native LTR G-rich ON template **T1** in the presence of different ligands namely, TMPyP4/DOX and TMPyP4+DOX. See Section 12 for details.

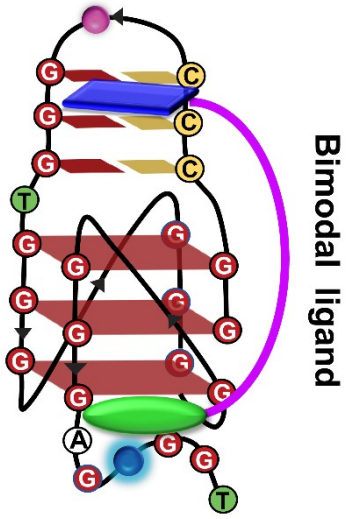

Fig. S30 Tailor-made bimodal ligand scaffolds composed of GQ and duplex binders could selectively interact with respective domains of LTR G-rich motif. The design of clamping linker (length and interaction partners) will be crucial in adding to the selectivity and location of binding within the GQ, hairpin and GQ-hairpin junction domains. Here, a representative mode of binding of the ligand scaffold is shown.

13. ^{31}P NMR of modified phosphoramidites

^{31}P NMR of **1a** (162 MHz, $CDCl_3$)

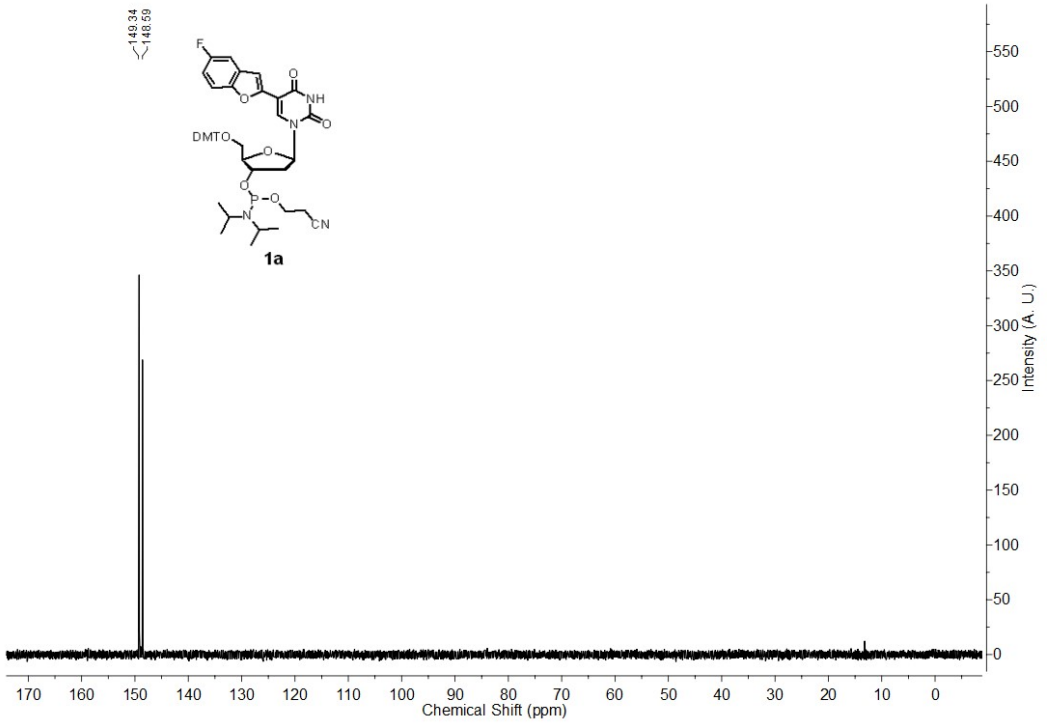

^{31}P NMR of **2a** (162 MHz, $CDCl_3$)

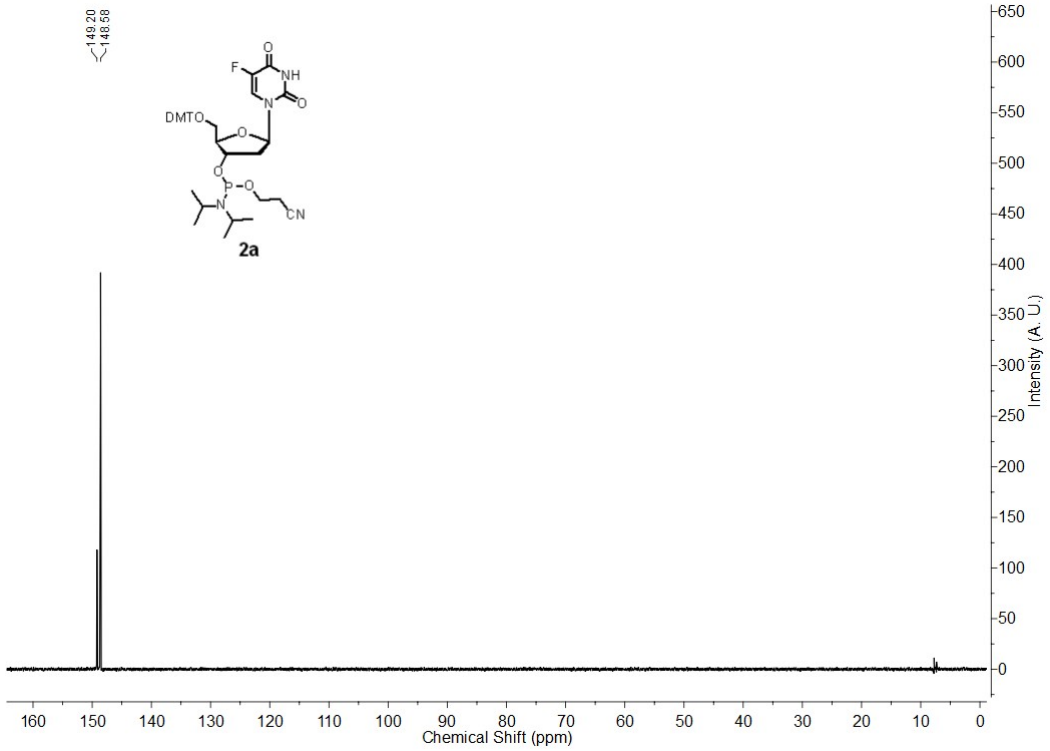

14. References

[S1] S. Manna, D. Sarkar, S. G. Srivatsan, *J. Am. Chem. Soc.* **2018**, *140*, 12622–12633.

[S2] L. Sacre, C. J. Wilds, *Eur. J. Org. Chem.* **2017**, 3003–3008.

[S3] A. Pandey, S. Roy, S. G. Srivatsan, *Chem. Asian J.* **2023**, *18*, e20230051.

[S4] P. Selenko, Z. Serber, B. Gadea, J. Ruderman, G. Wagner, *Proc. Natl. Acad. Sci. U. S. A.* **2006**, *103*, 11904–11909,

[S5] N. Yagi, K. Satonaka, M. Horio, H. Shimogaki, Y. Tokuda, S. Maeda, *Biotech Histochem*. **1996**, *71*, 123–129.

[S6] E. Butovskaya, B. Heddi, B. Bakalar, S. N. Richter, A. T. Phan, *J. Am. Chem. Soc.* **2018**, *140*, 13654–3662.

[S7] B. De Nicola, C. J. Lech, B. Heddi, S. Regmi, I. Frasson, R. Perrone, S. N. Richter, A.T. Phan, *Nucleic Acids Res.* **2016**, *44*, 6442–6451.

[S8] Gaussian 16, Revision B.01, M. J. Frisch, G. W. Trucks, H. B. Schlegel, G. E. Scuseria, M. A. Robb, J. R. Cheeseman, G. Scalmani, V. Barone, G. A. Petersson, H. Nakatsuji, X. Li, M. Caricato, A. V. Marenich, J. Bloino, B. G. Janesko, R. Gomperts, B. Mennucci, H. P. Hratchian, J. V. Ortiz, A. F. Izmaylov, J. L. Sonnenberg, D. Williams-Young, F. Ding, F. Lipparini, F. Egidi, J. Goings, B. Peng, A. Petrone, T. Henderson, D. Ranasinghe, V. G. Zakrzewski, J. Gao, N. Rega, G. Zheng, W. Liang, M. Hada, M. Ehara, K. Toyota, R. Fukuda, J. Hasegawa, M. Ishida, T. Nakajima, Y. Honda, O. Kitao, H. Nakai, T. Vreven, K. Throssell, J. A. Montgomery, Jr., J. E. Peralta, F. Ogliaro, M. J. Bearpark, J. J. Heyd, E. N. Brothers, K. N. Kudin, V. N. Staroverov, T. A. Keith, R. Kobayashi, J. Normand, K. Raghavachari, A. P. Rendell, J. C. Burant, S. S. Iyengar, J. Tomasi, M. Cossi, J. M. Millam, M. Klene, C. Adamo, R. Cammi, J. W. Ochterski, R. L. Martin, K. Morokuma, O. Farkas, J. B. Foresman, and D. J. Fox, Gaussian, Inc., Wallingford CT, 2016.

[S9] J. Wang, W. Wang, P. A. Kollman, D. A. Case, *J. Mol. Graph. Model.* **2006**, *25*, 247−260.

[S10] J. Wang, R. M. Wolf, J. W. Caldwell, P. A. Kollman, D. A. Case, *J. Comput. Chem.* **2004**, *25*, 1157−1174.

[S11] R. Galindo-Murillo, J. C. Robertson, M. Zgarbová, J. Šponer, M. Otyepka, P. Jurečka, T. E., Cheatham, III , *J. Chem. Theory Comput.* **2016**, *12*, 4114−4127.

[S12] S. Kumar, S. P. Pany, S. Sudhakar, S. B. Singh, C. S. Todankar, Pradeepkumar, P.I. *Biochemistry* **2022**, *61*, 2546−2549.

[S13] R. Salomon-Ferrer, A. W. Götz, D. Poole, S. Le Grand, R. C. Walker, *J. Chem. Theory Comput*. **2013**, *9*, 3878−3888.

[S14] A. W. Götz, M. J. Williamson, D. Xu, D. Poole, S. Le Grand, R. C. Walker, *J. Chem. Theory Comput.* **2012**, *8*, 1542−1555.

[S15] S. Le Grand, A. W. Götz, R. C. Walker, *Comput. Phys. Commun.* **2013**, *184*, 374−380.

[S16] D. A. Case, I. Y. Ben-Shalom, S. R. Brozell, D. S. Cerutti, T. E., Cheatham, III, V. W. D. Cruzeiro, T. A. Darden, R. E. Duke, D. Ghoreishi, M. K. Gilson, AMBER 2018; Univ. California: San Fr, **2018**; Vol. 2018.

[S17] D. R. Roe, T. E. Cheatham, *J. Chem. Theory Comput.* **2013**, *9*, 3084−3095.

[S18] W. Humphrey, A. Dalke, K. Schulten, *J. Molec. Graphics* **1996**, *14*, 33−38.

[S19] A. A. Tanpure, S. G. Srivatsan, *Nucleic Acids Res.* **2015**, *43,* e149.

[S20] M. Scalabrin, I. Frasson, E. Ruggiero, R. Perrone, E. Tosoni, S. Lago, M. Tassinari, G. Palù, S. N. Richter, *Sci. Rep.* **2017**, *7*, 45244.